MASTER THESIS

In Order to Obtain the

PROFESSIONAL MASTER

In

GEOGRAPHIC INFORMATION SYSTEMS & DATA SCIENCE (GIS)

Presented and defended by:

Eng. Samah Termos

TITLE:

Analyzing Damage in South Lebanon, and Developing a Comprehensive Assessment and Aid Platform

Supervisor

DR. CHADI ABDALLA

MS. HANINE SERHAN

Reviewers

Dr. AHMAD FAOUR

Lebanese University-Faculty of science

Acknowledgement

I would like to express my deepest gratitude to my advisors for their invaluable support and guidance throughout this research. I extend special thanks to Dr. Chadi Abdallah from CNRS and Miss. Hanine Serhan from Esri Lebanon for their expertise and encouragement, which were instrumental in completing this work.

I am also grateful to the team at CNRS, particularly Dr. Ghaleb Faour, for their unwavering support and for providing the resources and satellite imagery essential to this research. A heartfelt thanks to everyone who contributed to this effort, especially the CNRS-NCNE for their technical assistance and Esri Lebanon for their generous help and guidance.

I would like to thank my university, Lebanese University, and the faculty members who followed up with us throughout the year. My special thanks go to Dr. Ahmad Faour, the coordinator of this master, for his continuous encouragement and support.

On a personal level, I am profoundly grateful to my husband, Rida Alami, my children, and my parents and parents-in-law for their endless patience, love, and encouragement. My small family—my husband and kids—have been my strongest pillar of support throughout this journey.

Lastly, I wish to acknowledge my colleagues and friends for their motivation, and to all those who contributed in some way to the success of this thesis.

Abstract

The Israeli aggression on South Lebanon (October 2023 - November 2024) caused extensive destruction to buildings, severely disrupting livelihoods and recovery efforts. Traditional damage assessment methods are labor-intensive, time-consuming, and often fail to provide accurate, preliminary solutions for timely interventions. For instance, after the 2006 Lebanon war, damage assessments relied heavily on manual field surveys and visual inspections of aerial imagery, leading to delays in recovery planning.

This study presents an integrated approach that combine remote sensing, advanced AI methodologies, and multi-resolution satellite imagery for damage assessment. Sentinel-2 imagery was employed to enable rapid and large-scale evaluations, providing a broad overview of affected areas. In parallel, high-resolution satellite images facilitated precise, building-level damage detection through the implementation of SAMLoRA and change detection models, ensuring a detailed and accurate analysis of structural impacts.

The findings demonstrate that the SAMLoRA model achieved an accuracy of 0.9 in building-level damage detection, with no misclassified regions except for occasional errors in delineating building boundaries in densely populated areas. Moderate-resolution imagery enabled rapid identification of damage zones, with 80% of the zones accurately classified.

This research highlights the potential of combining AI and remote sensing for efficient war damage assessment. Future work should focus on expanding training datasets, refining model architectures, and leveraging field surveys for comprehensive validation. These advancements can enhance post-conflict recovery efforts by providing decision-makers with actionable insights, enabling effective prioritization of interventions and resource allocation.

Contents

List of Figures

List of tables

List of equations

Abbreviations

RS	Remote sensing
ML	Machine learning
DL	Deep learning
AI	Artificial intelligence
GEE	Google Earth Engine
NBR	Normalized burn severity
dNBR	Differential normalized burn severity
CNN	Convolutional Neural Networks
SAR	Synthetic Aperture Radar
SAMLoRA	Segment Anything Model with Low-Rank Adaptation
NDVI	Normalized Difference Vegetation Index
NIR	near-infrared
SWIR	Shortwave infrared
BUI	Built-up area
NDBI	Normalized Difference Building Index
RGB	Red Green Blue, True color image

Introduction

South Lebanon has endured repeated episodes of Israeli aggression over the past several decades, resulting in extensive infrastructure damage, severe disruptions to daily life, and prolonged challenges in recovery. The region has faced continuous challenges, including the destruction of residential and commercial properties, public utilities, and vital infrastructure. The Israeli offensives in 1978 and 1982, followed by a prolonged occupation until 2000 (MacQueen, 2013), as well as the 33 days destructive war of 2006. None the less, the renewed attacks since October 8, 2023, have further strained an already fragile infrastructure, affecting countless livelihoods.

In large scale damages, recovery efforts remain slow and fragmented especially in a country that lack resources and identified assessment frameworks.

Traditional methods of damage evaluation, such as visual interpretation of satellite imagery and ground field visits, are labor-intensive and time-consuming, requiring significant effort while often lacking efficiency. These approaches, while detailed, are limited by the need for extensive manpower and time, which can delay critical recovery efforts. Nonetheless, modern technologies can offer rapid and detailed assessments, providing decision-makers with accurate data to develop more effective and informed recovery plans.

Remote Sensing (RS) and Artificial Intelligence (AI) offer a transformative potential to address these longstanding challenges. RS enables the collection of high-resolution imagery over large geographic areas, while AI facilitates the analysis and interpretation of this data at unprecedented speed and accuracy. By integrating these technologies, it is possible to create efficient and systematic frameworks for assessing damage, prioritizing recovery, and allocating resources more effectively.

These tools enable efficient, systematic damage assessment and facilitate more effective recovery strategies. Recognizing the critical need for accurate assessments and prioritization in recovery efforts. This thesis, through the use of RS and AI, highlight the accuracy and efficiency of post-aggression damage assessments

Problem Statement

The Israeli aggression on South Lebanon commenced on October 8, 2023, and has resulted in the destruction of infrastructure including homes, businesses, roads, and public service utilities. Traditional damage assessment methods are time-consuming, resource-intensive, and limited to ground-based data, resulting in a major delay in recovery and response efforts.

The absence of a systematic, comprehensive assessment framework complicates the efforts to quantify damage and prioritize reconstruction. Additionally, delays in damage assessment hinder timely interventions, affecting the livelihoods of those impacted. This highlights the necessity of employing modern, efficient methodologies, such as satellite-based RS and AI technologies, to evaluate the extent of war damage and enable timely interventions (Risso, et al., 2024).

This research aims to tackle these challenges by developing an automated platform that leverages satellite imagery and AI to assess war-related damage to buildings in South Lebanon.

Objectives

The primary objective of this thesis is to develop an automated model that utilizes satellite imagery and AI to assess war damage in South Lebanon. Specifically, this research aims to:

1. Utilize RS data and deep learning algorithms to quantify the extent of damage caused by the Israeli aggression on South Lebanon.

2. Develop a user-friendly platform for conducting field visit assessments to enumerate the extent of damage and associated costs accurately.

3. Enable affected individuals to request assessment surveys for damaged properties through the platform.

Scope

The study focuses on war-related physical damage in South Lebanon caused by Israeli attacks, including destroyed or damaged buildings. The assessment is performed using high-resolution satellite imagery and DL models. This research does not cover economic or social damage assessments and is limited to damage that can be visually detected from satellite images.

1 Chapter 1: Literature Review

This chapter will provide an overview of the theoretical and practical advancements in damage assessment methodologies. It will delve into the evolution of key concepts, focusing on the combination of RS and machine learning technologies in this domain. The review explore the principles and techniques underpinning RS, including the use of satellite imagery and geospatial analysis to capture and interpret large-scale environmental and structural data.

Furthermore, the chapter assess how these technologies have been effectively utilized to tackle complex challenges in damage detection and recovery across diverse contexts, including natural disasters, urban conflicts, and post-war reconstruction. By identifying best practices, limitations, and gaps in existing methodologies, the chapter provide critical insights into how RS and machine learning have transformed traditional approaches to damage assessment.

1.1 Historical Context

The use of RS and AI for assessing damage in both conflict and natural disaster contexts has advanced significantly over the last few decades (Al Shafian & Hu, 2024). RS, involving the use of satellite and aerial imagery, has played a crucial role in rapidly assessing affected areas during conflicts and environmental disasters. RS has played a critical role in environmental disasters, such as hurricanes, floods, and earthquakes, by mapping impacted regions and supporting emergency response. For instance, during disasters like Hurricane Katrina and the 2010 Haiti earthquake, RS data enabled rapid assessments of damage, helping coordinate rescue and aid operations. These technologies have proven vital for supporting humanitarian efforts and guiding reconstruction activities in post-crisis scenarios.

In conflict zones, RS has been instrumental in providing timely and detailed assessments of the extent of destruction. For example, during the recent conflict in Kyiv, Ukraine, Sentinel-1 Synthetic Aperture Radar (SAR) and Sentinel-2 optical images were employed to assess building damage. By combining radar and optical imagery, researchers were able to overcome the challenges posed by cloud cover, ensuring consistent and reliable assessments of infrastructure damage. This approach highlights the effectiveness of using both SAR and optical data to provide comprehensive insights into conflict-related damage (Aimaiti, Sanon, Koch, Baise, & Moaveni, 2022).

RS has also played an essential role in monitoring and assessing damage from war disasters. For instance, in the Gaza Strip, time-series satellite RS has been used to assess the gradual increase in war damage, demonstrating the growing application of RS technologies in both conflict and natural disaster scenarios. The study by (Holail, et al., 2024) utilized time-series data from the LuoJia3-01 satellite to detect missile craters and evaluate building damage, demonstrating the effectiveness of combining DL with RS for monitoring of Israeli aggression. The research found a continuous increase in war damage, with a significant proportion of affected structures being residential and educational buildings. This approach highlights the potential of RS and AI to provide near real-time assessments, which are critical for timely humanitarian interventions and reconstruction planning.

Advancements in AI, particularly DL, have further enhanced the capabilities of RS for damage detection. Convolutional Neural Networks (CNNs) have become powerful tools for automating the classification and analysis of damage, reducing the need for manual interpretation. For example, the study by (Xu, Lu, Li, Zebo, & Zaytseva, 2019) demonstrated the use of CNNs for identifying building damage in both natural and conflict-related disasters, achieving high levels of accuracy. This underscores the importance of AI as a key component of modern damage assessment methodologies.

Additionally, (Liu, Yang, & Lunga, 2021) developed a two-phase object-based DL method for detecting changes in multi-temporal SAR images. This approach successfully addressed challenges such as speckle noise in SAR data, enhancing the accuracy of change detection, and distinguishing between real changes and false detections. Such innovations highlight the value of integrating DL techniques with traditional RS methods to improve the precision and efficiency of damage assessments.

AI-driven models like U-Net and Mask R-CNN have also been applied to datasets providing detailed classifications of building damage that are essential for coordinating effective aid distribution. These models have transformed traditional approaches, enabling faster and more scalable assessments in both conflict and disaster scenarios. The ability to automate damage detection and classification has significantly improved the speed and reliability of assessments, particularly in areas like South Lebanon, which require systematic recovery efforts due to repeated episodes of aggression (Zheng, Zhong, Wang, Ma, & Zhang, 2021).

These advancements illustrate the evolution of damage assessment methodologies from traditional manual techniques to advanced automated systems that leverage the power of AI and RS. Such developments have made damage detection faster, more accurate, and more scalable, ultimately providing essential support for regions like South Lebanon that require efficient, systematic solutions for recovery and aid distribution.

1.2 Remote Sensing

RS is the science of obtaining information about objects or areas from a distance, typically using satellite or aerial platforms. It involves capturing and interpreting electromagnetic radiation from the Earth's surface to analyze physical and environmental changes. As illustrated in Figure 1, remote sensing integrates various components such as satellites, drones, imagery, software, and classification techniques to provide a comprehensive understanding of Earth's systems. This technology enables the observation and monitoring of large and often inaccessible areas without direct contact, making it invaluable for numerous applications (Geography, 2024).

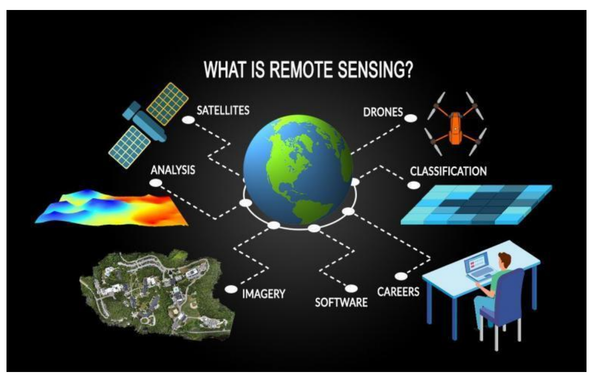

Figure 1: Overview of remote sensing, highlighting its key components and applications.

RS has found diverse applications across numerous fields. It is widely used for environmental monitoring, such as tracking deforestation, mapping urban expansion, monitoring water bodies, and assessing agricultural productivity. In disaster management, RS has proven invaluable for assessing the extent of natural disasters, such as hurricanes, earthquakes, floods, and wildfires, providing timely information for emergency response and recovery efforts (Ahmad, 2024). Additionally, in conflict zones, RS has been instrumental in assessing war-induced damage to infrastructure, allowing for rapid evaluation of destruction and aiding in the planning of reconstruction and humanitarian assistance (Joyce, Wright, Samsonov, & Ambrosia, 2024).

The benefits of RS include its ability to provide data over large spatial extents, offer frequent updates, and collect information in real-time or near real-time. This capability makes it particularly powerful in scenarios where traditional ground surveys are either impractical or impossible, such as during an active conflict or immediately after a natural disaster. The power of RS lies in its ability to monitor changes over time, identify patterns, and support data-driven decision-making (Campbell & Wynne, 2011) (Geography, 2024).

Multispectral Imaging is a key component of RS, where images are captured at different wavelengths across the electromagnetic spectrum. These wavelengths, typically including visible, near-infrared, and shortwave infrared bands, allow for the differentiation between various materials and land cover types. Multispectral images provide critical information for applications such as vegetation analysis, water quality monitoring, and urban planning (Richards, Sources and Characteristics of Remote Sensing Image Data, 2022).

Types of Resolutions in RS include: (Campbell & Wynne, 2011) (Lillesand, Kiefer, & Chipman, 2015):

- **Spatial Resolution**: Refers to the size of the smallest object that can be detected by the sensor, typically measured in meters. High spatial resolution is essential for detailed mapping and analysis.
- **Spectral Resolution**: Refers to the ability of a sensor to distinguish between different wavelengths. Higher spectral resolution enables the identification of specific materials based on their spectral signatures.
- **Temporal Resolution**: Refers to how often a sensor can capture data over the same location. High temporal resolution is critical for monitoring changes over time, such as deforestation or urban expansion.
- **Radiometric Resolution**: Refers to the sensitivity of a sensor to detect slight differences in energy. Higher radiometric resolution allows for more detailed analysis of the captured data.

1.2.1 Overview of Remote Sensing Indices

RS has emerged as a vital tool in assessing the impacts of war, offering a systematic and scalable approach to analyzing large areas affected by conflict. By leveraging satellite imagery, RS provides valuable insights into the spatial and temporal extent of damage, enabling rapid assessments. Among the many tools available in RS, indices such as the Normalized Difference Vegetation Index (NDVI), Normalized Burn Ratio (NBR), and their variations have proven highly effective in detecting changes in land cover, vegetation, and urban infrastructure (Lillesand, Kiefer, & Chipman, 2015).

The dNBR is a widely used RS index designed to quantify changes in vegetation and soil conditions caused by disturbances such as fires, deforestation, or war-related activities. It is calculated by subtracting the post-event Normalized Burn Ratio (NBR) from the pre-event NBR. The NBR itself is derived using the near-infrared (NIR) and shortwave infrared (SWIR) bands of satellite imagery, making it highly sensitive to changes in vegetation and soil reflectance (Key, Benson, & others, 2006).

Remote sensing has also been instrumental in damage assessment, especially when combined with AI technologies. AI has accelerated the analysis of RS data, enabling near real-time detection of damage and providing more precise classifications of affected areas. By automating the damage detection process, AI-driven models significantly reduce the time needed for assessments, which is crucial for effective response and recovery efforts.

1.3 Artificial Intelligence

AI represents a broad field of computer science focused on creating systems capable of performing tasks that typically require human intelligence, such as reasoning, learning, and decision-making (Russell & Norvig, 2021). Within AI, Machine Learning (ML) emerges as a critical subset that focuses on creating algorithms and statistical models, enabling machines to learn from and adapt to data without being explicitly programmed (Mitchell, 1997). ML relies on patterns and experiences to make predictions or automate decision-making, making it a foundational component of modern AI. Taking this a step further, Deep Learning (DL) is a subset of ML that artificial neural networks modeled after the human brain's structure and function.

DL excels in handling large datasets and extracting complex patterns, often outperforming traditional ML techniques in areas like computer vision, natural language processing, speech recognition, and autonomous systems (LeCun, Bengio, & Hinton, Deep learning, 2015). Together, these interconnected fields represent a hierarchy of approaches that progressively enhance the capability of machines to emulate human-like intelligence, paving the way for transformative applications across various domains.

1.4 Machine learning for image analysis

Machine learning (ML) is a branch of AI that enables systems to learn from data, identify patterns, and make decisions with minimal human intervention. It began in the mid-20th century, with early uses primarily focused on statistical pattern recognition and simple algorithms for data analysis (Samuel, 1959) . Arthur Samuel, a pioneer in the field, developed one of the first machine learning applications: a program that could play checkers and improve its performance through experience.

Since then, machine learning has evolved significantly, becoming integral to a wide range of applications, from natural language processing and recommendation systems to medical diagnostics. In recent years, machine learning has also found widespread use in RS, especially for image analysis tasks such as land cover classification, change detection, and damage assessment (Adegun, Viriri, & Tapamo, 2023).

DL, a subset of machine learning, has been particularly powerful in this context, enabling the extraction of complex features from high-resolution satellite imagery, which is crucial for detecting and analyzing damage in both natural disaster and conflict scenarios. As illustrated in Figure 2, deep learning automates feature extraction and classification into a single process, unlike traditional machine learning, which relies on separate preprocessing, feature extraction, and selection stages.

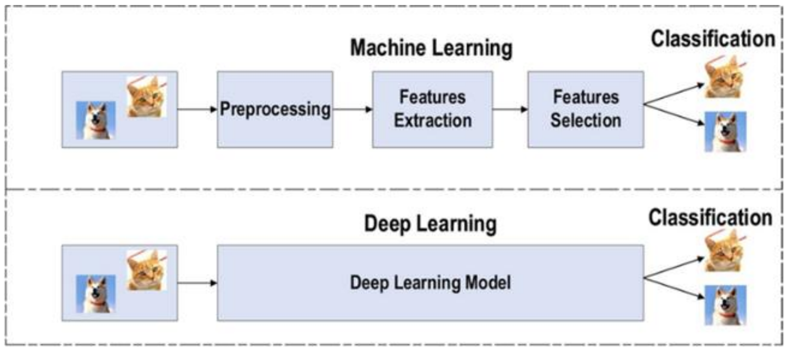

Figure 2: Machine learning and deep learning workflows for image classification.

1.5 Deep Learning and Segmentation

Computer vision, a branch of AI, focuses on enabling computers to analyze and interpret visual data from the real world. This field encompasses a range of techniques aimed at extracting meaningful information from images or videos, such as object detection, image classification, and scene analysis (Forsyth & Ponce, 2002).

DL, a subset of machine learning, is a technique used in computer vision that involves the use of artificial neural networks with many layers to learn representations from data. It was first conceptualized in the 1980s, but advancements in computational power, availability of large datasets, and improved algorithms have led to its widespread adoption in recent years (LeCun, Bengio, & Hinton, Deep Learning, 2015). DL has been applied to various applications, including natural language processing, autonomous vehicles, and medical image analysis, demonstrating its versatility and power (Ali Eli & Ali, 2024).

In image analysis, different DL types can be used, the most famous ones are: Convolutional Neural Networks (CNNs), which are particularly effective for feature extraction from images, Recurrent Neural Networks (RNNs) for sequential data analysis, and Generative Adversarial Networks (GANs), which are used to generate synthetic data and enhance image quality.

Object detection and segmentation are two critical techniques in computer vision, each with unique applications and advantages, particularly in fields like RS and damage assessment (Girshick, Donahue, Darrell, & Malik, 2014).

Object detection is a computer vision method used to identify and localize multiple objects within an image (MathWorks, 2024). It plays a pivotal role in applications such as autonomous driving, security surveillance, and RS. Its primary advantage lies in its ability to detect specific features or entities within an image, enabling targeted analysis. For instance, in a post-disaster scenario, object detection can be employed to identify damaged buildings or vehicles. This technique is highly efficient, providing vital information about the number, type, and location of detected objects, which is essential for effective decision-making (Kaur & Singh, 2022).

Segmentation, particularly in RS, involves categorizing each pixel in an image into a specific class, a process known as pixel detection (Zhang, Jiang, Zheng, & Yao, 2023). The most common form used in damage assessment is semantic segmentation, where each pixel is assigned a class label, such as building, road, or vegetation. Unlike object detection, which focuses on identifying and localizing entire objects, segmentation offers per-pixel accuracy, allowing for precise classification of areas affected by damage. This detailed understanding is invaluable for assessing the extent and severity of damage (Lv, Shen, Lv, Li, & Shi, 2023).

The main distinction between these two techniques lies in their focus and level of detail. Object detection identifies and localizes whole objects within an image, providing broader information about their presence and location. In contrast, segmentation classifies each individual pixel, creating a more comprehensive understanding of the entire scene (Garcia-Garcia, Orts-Escolano, Oprea, Villena-Martinez, & Garcia-Rodriguez, 2017). Together, these methods complement each other, offering critical insights for a wide range of applications, from disaster response to land cover classification.

These advancements in DL have made it possible to analyse RS imagery more accurately and efficiently, providing significant benefits in damage assessment and recovery planning.

1.6 Related Work

1.6.1 Traditional damage assessment

Traditional damage assessment has typically relied on manual surveys, ground-based inspections, and visual interpretation of aerial imagery. These methods, although providing in-depth localized assessments, are time-consuming and labor-intensive, often requiring a significant amount of human resources. Traditional techniques, such as visual analysis of high-resolution satellite images, have been commonly used in damage assessment, particularly during the early conflicts of the 20th century. However, these approaches have significant limitations in terms of scalability and efficiency, particularly in large-scale disaster or conflict scenarios where rapid assessments are crucial.

Ground-based surveys provide detailed, localized data but are constrained by accessibility issues, especially in conflict zones or areas affected by natural disasters where infrastructure may be severely damaged. Aerial imagery visual interpretation, while providing a broader view, requires extensive manual analysis by experts, making it susceptible to human error and inconsistencies. Additionally, these methods are limited by the availability of field personnel and are highly dependent on favorable conditions for data collection.

The accuracy of traditional assessments is also affected by the subjectivity of manual interpretation, which can lead to variability in results. For instance, during the 2005 Pakistan earthquake and the 2010 Haiti earthquake, manual visual assessment of satellite imagery was used extensively, but the process was slow and could not provide the timely information needed for effective crisis response. The dependence on human intervention often delayed the process of damage quantification, thus delaying the delivery of aid and reconstruction efforts. Due to these challenges, there has been a growing interest in utilizing automated and scalable solutions such as RS combined with AI to improve the speed and reliability of damage assessment (Ahmad, 2024).

1.6.2 AI-based assessment methods

AI-based damage assessment methods have significantly transformed the traditional approach to analyzing damage from conflicts and natural disasters (Voigt, et al., 2007). One of the primary advantages of using AI is its ability to handle large datasets, which makes it particularly effective for assessing damage on a large scale. Recent advancements in machine learning, specifically DL, have enabled the automation of damage detection through RS, greatly improving the speed and accuracy of assessments (Xu & Khaitan, 2020).

For instance, DL models such as Convolutional Neural Networks (CNNs) and U-Net have been extensively used in damage detection tasks, providing highly accurate results by automatically learning features from satellite imagery. For example, a study by (Aimaiti, Sanon, Koch, Baise, & Moaveni, 2022) in Kyiv utilized Sentinel-1 and Sentinel-2 imagery combined with machine learning models to assess building damage. This AI-driven approach enabled efficient, timely assessments that were not feasible with traditional methods.

In situations such as the Israeli aggression in the Gaza Strip, (AI) combined with time-series satellite RS was used to evaluate the progression of war damage, allowing for near real-time monitoring of affected areas (Holail, et al., 2024). The use of AI in this context helps overcome challenges like cloud cover and other environmental factors that often hinder RS efforts. DL models also have the ability to identify subtle changes and patterns in the data, making them particularly useful in detecting damage that may not be immediately visible to the human eye.

Comparatively, AI-based assessment methods outperform traditional approaches by automating the damage detection process, significantly reducing the need for manual interpretation. AI's ability to automatically extract features from imagery minimizes human error and ensures consistent results. Unlike traditional ground surveys and manual image analysis, AI-driven damage assessments are not only faster but also more scalable. In situations like the 2015 Nepal earthquake, where a rapid response was critical, AI has demonstrated the capacity to generate detailed damage maps much faster than ground-based inspections (Garcia-Garcia, Orts-Escolano, Oprea, Villena-Martinez, & Garcia-Rodriguez, 2017).

The integration of AI into damage assessment processes not only enhances the speed of analysis but also reduces the dependency on manual interpretation, which is prone to human error and inconsistencies. Models like Mask R-CNN have been successfully applied to classify damage levels in various building structures, facilitating a more accurate and consistent evaluation of damage (Zheng, Zhong, Wang, Ma, & Zhang, 2021). These advancements highlight the importance of AI-based solutions in providing rapid, reliable assessments that are critical for effective disaster response and reconstruction efforts

Moreover, recent advancements such as Transformer-based architectures have also started to impact the field of damage assessment. Transformer models, initially developed for natural language processing, are being adapted to process image data for damage detection. They provide a new level of accuracy, especially when dealing with complex environments that have multiple types of damage (Z. Xu, Lu, Li, Khaitan, & Valeriya, 2021).

According to an analysis by the New Security Beat, early conflict damage assessments using AI have shown great promise in accelerating relief efforts by ensuring that aid organizations receive timely and accurate information (Weinthal, 2024). Furthermore, a report from (Planitz, 1997) suggests that traditional damage assessments are limited in speed and scalability, particularly during large-scale disasters, which is where AI models excel. Studies also show that post-war building damage detection using DL can offer enhanced precision in analyzing affected structures, reducing the time needed for manual survey efforts (Bashir Khajwal, Cheng, & Noshadravan, 2022). Engineering DL methods on automatic damage detection can increase the accuracy and reliability of assessments during extreme events, making it a promising area for ongoing research (Bai, Zha, Sezen, & Yilmaz, 2022). The use of a multi-view convolutional neural network, as shown in recent studies, has greatly expanded the effectiveness of AI-based methods in infrastructure damage detection (Xia, et al., 2023). Another notable study explores the use of Mask-RCNN and Transformers in assessing infrastructure affected by warfare, showing improved generalization and scalability of these models (Bai, Zha, Sezen, & Yilmaz, 2021).

These advancements in AI-based methods highlight their importance in enhancing damage detection, ensuring effective resource allocation, and expediting recovery efforts. Such techniques make it possible to deliver a quick yet thorough understanding of affected areas, which is critical for regions like South Lebanon that face repeated violence and ongoing infrastructure challenges.

A- Overview and Foundations of damage detection using Pixel Classification

Pixel classification model is designed to assign a specific label to each pixel in an image based on its features. These models use machine learning or DL techniques to analyse spatial, spectral, and contextual information from images. This approach is particularly valuable for applications such as land cover mapping, damage assessment, and environmental monitoring.

DL models for pixel classification are exceptionally effective, leveraging their ability to automatically extract spatial, spectral, and contextual features from input data. These models excel in handling the high dimensionality of multi-band satellite and aerial imagery, making them particularly suited for analysing complex and heterogeneous datasets. DL-based approaches are highly scalable, capable of processing extensive geographic areas and accommodating imagery of varying resolutions. By learning directly from raw data, these models not only capture intricate relationships and patterns but also enhance pixel-level classification accuracy. With sufficient training data, they demonstrate strong generalizability across diverse regions and conditions, establishing themselves as robust and versatile tools for a wide range of RS tasks (Ma, et al., 2019) (Zhu, et al., 2017).

The labelled data structure used for high-level damage assessment using pixel classification typically consists of input imagery paired with corresponding ground truth masks. The input images are high-resolution satellite or aerial imagery, often multi-band (e.g., RGB, near-infrared), that capture the affected areas. The ground truth masks are raster layers where each pixel is assigned a class label representing its status, such as "damaged," "undamaged," or "background" (Shorten & Khoshgoftaar, 2019).These masks are usually created through manual annotation or semi-automated techniques, often guided by expert knowledge and field validation. To ensure alignment, both the input images and labels must share the same spatial resolution and extent. The labelled data is stored in formats such as GeoTIFF, PNG, or NumPy arrays, allowing seamless integration with DL frameworks. The dataset is usually split into training, validation, and test subsets to train the model, evaluate its performance, and generalize its application to unseen data. Pre-processing steps, such as normalization and data augmentation, are often applied to improve model robustness and handle class imbalance, ensuring accurate pixel-level classification for high-level damage assessments (Zhu, et al., 2017).

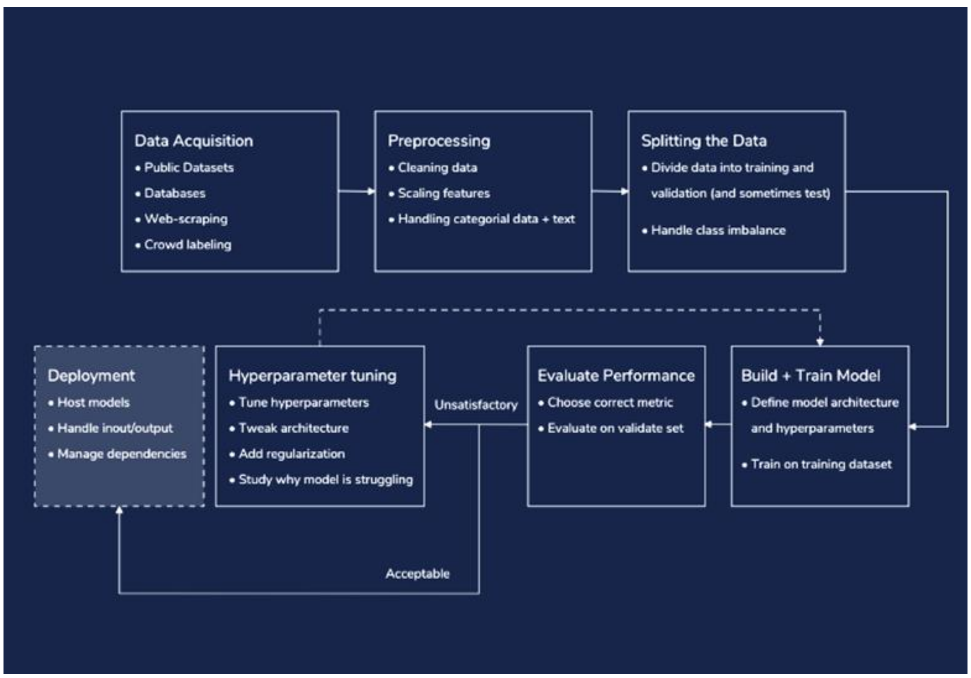

Figure 3: Workflow for DL Model Development

The workflow as shown in Figure 3of pixel classification models generally begins with data pre-processing, which includes steps like correcting the image for atmospheric effects, normalizing reflectance values, and aligning images from multiple sources to ensure consistency. Following this, a training phase uses labelled pixels (ground truth) to teach the model how to associate certain pixel characteristics with corresponding classes, such as "damaged buildings," "vegetation," or "water" (Richards, 2022). While traditional (ML) models rely on manually engineered features, (DL) models automatically extract relevant features through their network layers. After the model has been trained, it performs classification by assigning each pixel a class label based on the learned patterns and calculated probabilities. To further refine the results, post-processing techniques—such as smoothing or morphological operations—are applied to the final output, enhancing the overall accuracy and clarity of the classification (LeCun, Bengio, & Hinton, 2015).

Pixel classification models, when implemented with advanced techniques such as SAMLoRA or Change Detector architectures, can provide highly accurate and efficient analysis for a variety of RS applications. Their ability to integrate spatial, spectral, and contextual features makes them indispensable tools in geospatial science and AI-driven imagery analysis.

B- Overview of SAMLoRA

SAMLoRA (Segment Anything Model with Low-Rank Adaptation) is a modern DL framework designed to enhance the efficiency and performance of segmentation tasks, particularly in RS and damage detection. The foundation of SAMLoRA is based on the integration of two key components: the Segment Anything Model (SAM) and Low-Rank Adaptation (LoRA).

The Segment Anything Model (SAM) was initially developed as a transformer-based image segmentation architecture aimed at solving the challenges of segmenting objects in diverse, unstructured environments. SAM leverages attention mechanisms to capture both local and global context, allowing it to identify and delineate objects in images without requiring extensive manual annotations. SAM has been applied in various fields such as RS, medical imaging, and independent driving, where rapid and accurate segmentation is critical.

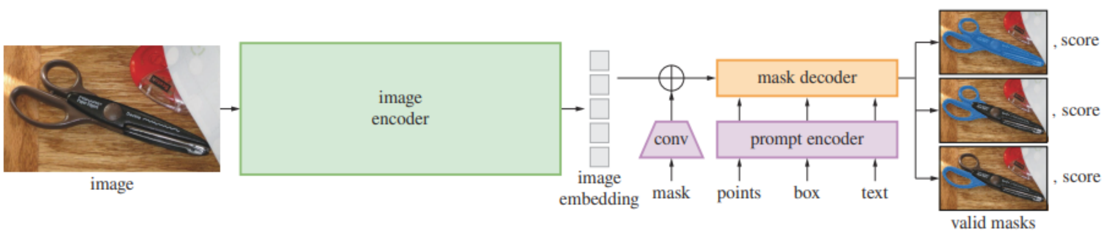

Figure 4: Segment Anything Model (SAM) architecture overview

Low-Rank Adaptation (LoRA) emerged as a technique to improve the efficiency of large pre-trained models by reducing computational complexity. LoRA achieves this by approximating the weight matrices of the model with low-rank updates, significantly reducing memory and computational overhead while maintaining or even improving model performance. LoRA has become a popular approach in fine-tuning pre-trained models, making them more adaptable to specific tasks with smaller, task-specific datasets.

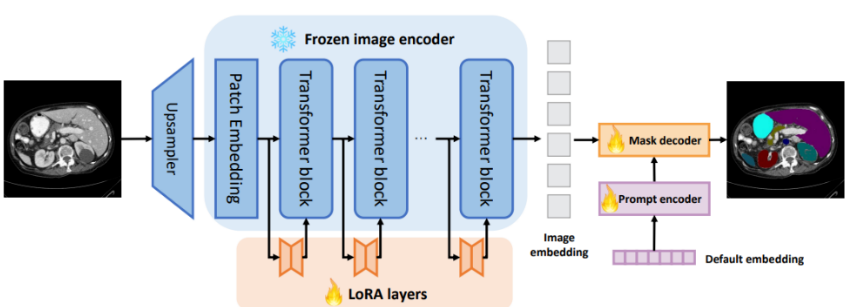

Figure 5: SamLoRA architecture overview

The integration of SAM and LoRA in SAMLoRA was motivated by the need to enhance segmentation tasks for RS applications while maintaining computational efficiency. SAMLoRA enables high-quality pixel-level classification with improved adaptability and scalability, making it suitable for large-scale damage detection in satellite imagery.

The integration of SAM with LoRA creates a hybrid model that combines the strengths of both components. SAM, with its transformer architecture and attention mechanisms, excels at segmenting complex objects in diverse environments. However, DL models like SAM can be computationally expensive and require large amounts of labeled data. This is where Low-Rank Adaptation (LoRA) comes into play (Prado Osco, et al., 2023).

LoRA adapts SAM by reducing its computational burden through low-rank updates to its weight matrices. Rather than re-training the entire model from scratch, LoRA fine-tunes specific layers of SAM, making the model more efficient for targeted tasks like damage detection in satellite imagery. This combination allows SAMLoRA to perform rapid, pixel-level classification on large datasets without requiring vast amounts of computational resources.

SAMLoRA has demonstrated its potential in a variety of applications, particularly in RS and damage detection. One notable use case is post-disaster damage assessment, where SAMLoRA can accurately detect and classify damaged areas, such as collapsed buildings, destroyed roads, or vegetation loss, from high-resolution satellite or aerial imagery. Similar studies have also explored integrating attention-based models with low-rank techniques. For instance, (Prado Osco, et al., 2023) discussed the use of transformer-based models for segmentation tasks in RS, while the study "SAMRS: Scaling-up RS Segmentation Dataset with Segment Anything Model"demonstrates SAMLoRA's effectiveness in generating large-scale RS segmentation datasets (Wang, et al., 2023).Other studies, such as (Zhu, et al., 2017), highlighted the effectiveness of DL in RS and damage detection, laying the groundwork for SAMLoRA’s application in the field.

The dataset used for SAMLoRA classification involves high-resolution satellite imagery paired with labeled feature masks for the same spatial extent. The satellite imagery serves as the input data, typically containing multi-spectral or RGB channels that capture detailed spatial and spectral information about the area of interest. The labeled feature masks, often created through manual annotation or semi-automated techniques, are raster layers where each pixel is assigned a specific label, such as "damaged," "undamaged," or "background." These labels serve as the ground truth for training the model and aligning predictions during evaluation.

To ensure compatibility with the SAMLoRA architecture, the imagery and corresponding labels are preprocessed into smaller, fixed-size patches (e.g., 256x256 pixels). This patch-based approach facilitates efficient processing, enabling the model to learn local spatial patterns and contextual information effectively. The patch extraction ensures that each patch includes both the satellite imagery and the associated labeled data for the same spatial extent, maintaining alignment between input features and ground truth. This approach also enables the model to handle large-scale datasets by dividing them into manageable segments, which is crucial for high-resolution imagery. Additional preprocessing steps, such as normalization of pixel values and augmentation techniques like rotation, flipping, or scaling, are applied to improve the model's robustness and generalization. By meticulously preparing and preprocessing the dataset, SAMLoRA can efficiently learn to classify pixels, leveraging its capabilities for high-level damage assessment and other pixel classification tasks.

C- Overview of Change detection

Change detection using DL has emerged as a transformative approach for analyzing differences between pre- and post-event images, particularly in applications such as disaster response and damage assessment. By leveraging neural networks to process spatial and temporal image data, DL models achieve unparalleled accuracy and scalability compared to traditional methods.

DL-based change detection first gained prominence with the introduction of Convolutional Neural Networks (CNNs) in the early 2010s, which enabled automated feature extraction from RS imagery. Early models, such as the Fully Convolutional Network (FCN) and Siamese networks, demonstrated the ability to identify structural changes like building damage and land use alterations (Chen et al., 2020). In 2016, approaches integrating U-Net architectures provided enhanced pixel-level classification accuracy, making them particularly effective for detailed damage mapping (Ronneberger, Fischer, & Brox, 2015).

Several projects have showcased the potential of DL in change detection. For example, during the Indonesia earthquake, optical flow-based models detected changes in collapsed buildings and debris zones, providing critical insights for rescue operations (Qiao, Wan, Xu, Li, & He, 2020). Similarly, a study on the Shishper Glacier in Pakistan applied CNN-based methods to identify temporal changes in glacial dynamics, proving the versatility of these models beyond disaster contexts (Jamil, et al., 2019). Recent advancements in conflict zone analysis, such as damage assessment in Ukraine using high-resolution satellite images, employed Siamese networks to classify building-level changes with high precision (Aimaiti, Sanon, Koch, Baise, & Moaveni, 2022).

DL models offer significant advantages in change detection, particularly in automation, scalability, and adaptability. These models eliminate the need for manual feature engineering by automatically extracting complex patterns from imagery, resulting in superior accuracy and efficiency (Zhu, et al., 2017). Their scalability enables the processing of large volumes of data, making them well-suited for analyzing extensive geographic regions and conducting long-term monitoring (Chen et al., 2020). Additionally, DLtechniques such as transfer learning enhance adaptability, allowing models to perform effectively even with limited labeled datasets, thereby reducing the dependency on extensive training data (Shorten & Khoshgoftaar, 2019).

Change detection techniques in DL face several challenges, including data limitations, computational intensity, and error sensitivity. High-quality pre- and post-event imagery with minimal inconsistencies is essential for accurate analysis, yet such data can be difficult to acquire in real-world scenarios, especially in disaster or conflict settings (Lu et al., 2004). Additionally, the training and deployment of models require substantial computational resources, which can restrict their accessibility in resource-constrained environments (Jamil et al., 2019). Variations in image acquisition conditions, such as differences in angle, lighting, and shadow, further complicate the process, making advanced preprocessing techniques necessary to ensure reliable performance (Qiao, Wan, Xu, Li, & He, 2020).

1.6.3 Drawbacks of AI-Based Methods

Despite these advancements, AI-based damage assessment methods have certain limitations. One significant drawback is the dependence on high-quality data. AI models require large volumes of accurately labeled training data, which can be challenging and time-consuming to obtain, particularly in conflict or disaster zones where resources are limited and accessibility is restricted.

Another limitation is the challenge of data diversity. AI models may struggle to perform accurately in new or untrained environments due to insufficient diversity in the training datasets. This can lead to errors in areas with unique damage patterns or conditions that were not represented in the training data.

Computational intensity also presents a notable challenge. Training and deploying AI models demand significant computational resources, including high-performance GPUs, which may not be accessible in regions with limited infrastructure.

Environmental factors further complicate the application of AI-based methods. Issues such as cloud cover, lighting variations, and shadows in satellite imagery can hinder the accuracy of these models. Extensive pre-processing is often required to address these challenges, adding complexity to the workflow.

Finally, the risk of overfitting is a concern. AI models, particularly those based on deep learning, can overfit to the specific features of the training data, reducing their ability to generalize to unseen datasets. This affects the reliability of the models in real-world applications (Hou & Li, 2024).

1.7 Gap Analysis

In existing damage assessment approaches, significant limitations hinder their effectiveness. Traditional methods, such as manual surveys and ground-based inspections, are time-consuming, labor-intensive, and often impractical for large-scale and rapid assessments, especially in conflict zones. Although AI-based methods have improved the efficiency of damage detection, they still face challenges, such as the requirement for extensive labeled data for training, difficulties in adapting models to diverse environments, and limitations in distinguishing between different damage types accurately.

This work addresses these challenges with a two-phase approach: medium-resolution imagery for rapid large-area screening, followed by high-resolution imagery for detailed assessment of critical zones. By integrating advanced AI models with adaptive learning, this scalable solution enables precise damage assessments and timely interventions, particularly in South Lebanon, where systematic recovery efforts are crucial.

2 Methodology

2.1 Study Area

Lebanon is a small historically country located on the eastern shore of the Mediterranean Sea in Western Asia. It covers an area of approximately 10,452 square kilometers, making it one of the smallest countries in the region. The country shares borders with Syria to the north and east, and Occupied Palestine to the south. The borderline between Lebanon and the occupied land in Palestine is approximately 49 miles (78.8 kilometers) long. Additionally, the boundary between Lebanon and the occupied land in Syria (Golan Heights) contributes to the total length of what is called the 'Blue Line,' which spans approximately 130 km between Lebanon and the occupied land.

The violence that occurred from October 8, 2023, to November 27, 2024, resulted in extensive building damage across Lebanon. Airstrikes targeted various regions, causing severe destruction in urban and suburban areas, including Beirut's suburbs, Baalbek, and the Bekaa Valley. The intensity and extent of damage varied across the country, with the southern region experiencing the most significant destruction. In many areas, residential and commercial buildings were reduced to rubble, leaving thousands homeless and disrupting local economies. The airstrikes in regions like Baalbek and the Bekaa Valley caused widespread damage to vital infrastructure and densely populated areas, while the outskirts of Beirut suffered substantial harm due to repeated bombardments (INTERSOS, 2024).

South Lebanon, however, faced unparalleled devastation, particularly in areas close to the Blue Line. This region endured catastrophic damage, exacerbated by a large-scale land invasion. The invasion involved widespread destruction to facilitate the movement of military tanks and vehicles, leading to the complete or partial destruction of entire villages. Towns such as Bint Jbeil, Aita al-Shaab, and Khiam suffered extensive building damage, including residential structures, public facilities, and utilities. As illustrated in Figure 6, the intensity of destruction increased closer to the border, highlighting the region's strategic importance during the violence.

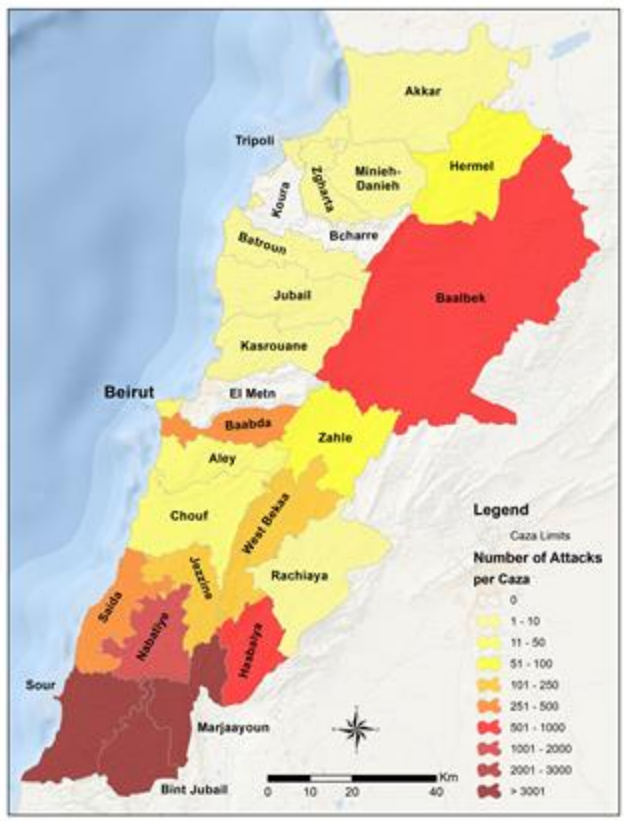

Figure 6: Map showing total number of attacks per caza

South Lebanon was chosen as the study area for this thesis due to the scale of building damage it experienced as shoen in Figure 6. The focus on this region provides a comprehensive setting for analyzing the impact of the violence on residential and public infrastructure. This study utilizes high-resolution satellite imagery to assess and map the extent of building damage in South Lebanon.

2.2 Materials

2.2.1 Satellite Imageries

A. Sentinel

Sentinel-2 imagery served as the primary data source for regional-scale analysis due to its moderate spatial resolution (10 meters) and multi-spectral capabilities. These characteristics strike a balance between spatial coverage and resolution, making Sentinel-2 suitable for monitoring post-conflict recovery. Its five-day revisit time enables frequent updates, while key spectral bands, including Red, Near-Infrared (NIR), and Shortwave Infrared (SWIR), enhance the detection of structural and vegetation changes. The imagery is freely available through the Copernicus Open Access Hub, ensuring cost-efficiency and accessibility.

For this study, Sentinel-2 imagery from three specific dates was selected to enhance temporal diversity for damage detection analysis. The details of these images, including acquisition dates and file names, are summarized in Table 1.

Sentinel-2 Image Dates	**Name of Image**
15th November 2024	S2B_MSIL2A_20241115T082119_N0511_R121_T36SYB_20241115T094613
30th November 2024	S2A_MSIL2A_20241130T082311_N0511_R121_T36SYB_20241130T112551
5th September 2024	S2B_MSIL2A_20241205T082229_N0511_R121_T36SYB_20241205T093809

Table 1:Sentinel-2 Imagery Dates for Damage Detection Analysis

The Sentinel-2 imagery zone, as shown in Figure 7, fully covers the study area in the southern region of Lebanon. This specific zone encompasses all regions required for the analysis, with no need for additional imagery from other zones. The three selected images used for this study share the same spatial extent,

However, the 10-meter resolution of Sentinel-2 presents challenges in identifying smaller-scale damage or subtle structural changes. These limitations emphasize the need for complementary higher-resolution satellite imagery for detailed assessments

Figure 7: The area covered by Sentinel-2 imagery

B. High-Resolution Satellite Imagery

To address the limitations of Sentinel-2 imagery, high-resolution satellite imagery with a spatial resolution of 0.3 meters was employed for detailed building-level damage detection in South Lebanon. This high-resolution dataset consisted of two sets of images: a pre-war dataset from 2023, sourced from Bing Satellite Imagery, and a post-war dataset from 2024, provided by OnGeo™ Intelligence. The pre-war imagery served as a baseline for identifying changes, while the post-war imagery, captured between October 28 and December 5, 2024, highlighted the damage caused by the war. Together, these datasets enabled a comprehensive analysis of structural changes.

The Bing Satellite Imagery dataset, captured in 2023, served as the pre-war baseline for this analysis, providing essential data to establish the initial condition of structures before the conflict. This free dataset features a high spatial resolution of 0.3 meters, enabling detailed visualization of building features and infrastructure. Unlike other datasets, Bing Satellite Imagery offers complete coverage of Lebanon, including the study area in South Lebanon. This comprehensive coverage ensured that all regions of interest within the study area were included, providing a reliable foundation for comparing pre-war and post-war conditions. The high resolution and extensive geographic scope of the imagery made it particularly valuable for identifying structural changes and quantifying damage caused by the war.

The OnGeo™ imagery included 29 cloud-free images, covering selected regions in South Lebanon with a total area of 157.53 square kilometers. While this imagery did not provide complete coverage of the study area, it encompassed regions with diverse data characteristics and represented the only accessible high-resolution datasets for this analysis. The selected regions included a mix of urban and suburban areas severely impacted by the conflict, as shown in the spatial footprints in Figure 8. The high resolution of the imagery facilitated precise analysis and reliable detection of structural damage, addressing the challenges posed by Sentinel-2's moderate resolution.

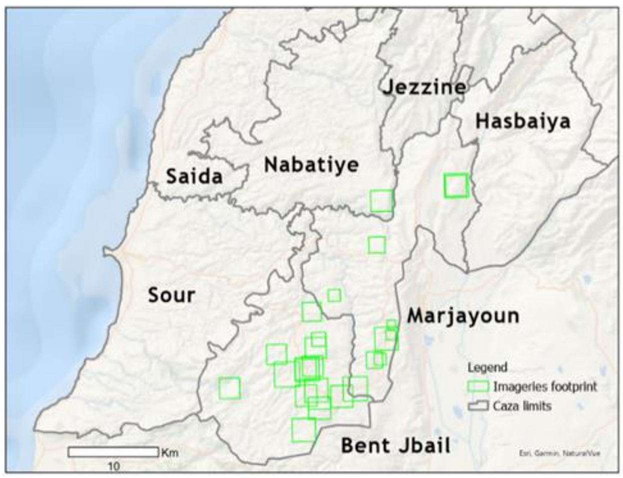

Figure 8: Map illustrating the spatial footprints of high-resolution satellite imagery captured during and post-war.

2.2.2 Software and Capacity

This study utilized a range of software tools and computational resources to ensure effective data analysis, model training, and damage assessment. The selection of software and hardware was tailored to handle the complexity and volume of satellite imagery data while supporting advanced machine learning workflows.

A. Software Tools

ArcGIS Pro was employed for geospatial data preprocessing, including georeferencing, and generating training datasets. The Export Training Data tool was important in structuring image chips and corresponding labels required for deep learning models. Additionally, ArcGIS Pro's analytical capabilities were used to visualize and validate results.

Python, along with its specialized libraries, served as the foundation for the deep learning workflows in this study. A key library, arcgis.learn, was employed for training pixel classification models such as the Change Detector and SAMLoRA models. This library provided seamless integration between geospatial data and deep learning processes, making it indispensable for building and deploying AI models. Additionally, PyTorch and TensorFlow were utilized for implementing and optimizing the deep learning models, offering robust frameworks for handling complex computational tasks and improving model performance.

Survey123 was used to design and deploy digital field data collection forms. These forms should be used for systematic gathering of supplementary information from affected areas, offering valuable insights additionally to what could be derived from satellite imagery or AI models.

Google Earth Engine (GEE) was used in calculating remote sensing indices. Its cloud-based platform allowed efficient access to and processing of Sentinel-2 imagery, streamlining tasks such as atmospheric correction, cloud masking, and spectral analysis.

Sentinel Hub’s APIs and platform were utilized to efficiently download Sentinel-2 imagery for this study. The platform provided seamless access to multi-temporal and multi-spectral datasets.

B. Capacity

The computational demands of training deep learning models were addressed using two GPU-enabled systems with varying capabilities, as summarized in Table 2. Computer One, equipped with an NVIDIA GPU (8 GB VRAM) and 32 GB RAM, was primarily used for initial data preprocessing and lightweight model experimentation. In contrast, Computer Two, featuring an NVIDIA Tesla V100 GPU (24 GB VRAM) and 960 GB of RAM, handled the more intensive tasks of model training and optimization.

Component	Computer one	Computer two
GPU	NVIDIA (8 GB VRAM)	Two NVIDIA Tesla V100 (24 GB VRAM)
CPU	Intel Xeon Processor (2.6 GHz)	Intel Xeon Silver 4114 @ 2.20 GHz (2 CPUs)
RAM	32 GB	960 GB
Operating System	64-bit, x64-based architecture	64-bit, x64-based architecture

Table 2: Specifications of the computational systems used for deep learning workflows.

2.3 Methods

2.3.1 Rapid Assessment Using RS Indices

Different indices were calculated to assess their effectiveness in detecting damage, including the difference in the Normalized Difference Building Index (dNDBI) (Zha, Gao, & Ni, 2003) and the changes in the Built-Up Area Index (BUI) (Xu H. , 2007). These indices, often used to identify alterations in built-up areas and infrastructure, were expected to highlight damage with reasonable accuracy. However, the results indicated that these indices were not sufficiently sensitive or specific in capturing the extent of damage in the study area. This limitation could be attributed to factors such as the spectral similarity of damaged and undamaged built-up areas or the relatively subtle spectral changes associated with structural damage. In contrast, the Differenced Normalized Burn Ratio (dNBR), which is traditionally used for burn severity analysis, demonstrated a higher level of reliability in identifying damage. The dNBR proved capable of distinguishing damage-related changes effectively, making it a more suitable choice for damage assessment in this context.

When analysing war damage over a time period exceeding one year, the temporal gap introduces significant challenges to the use of traditional RS indices. Environmental and anthropogenic factors, such as seasonal variations, vegetation regrowth, urban redevelopment, or unrelated land-use changes, can mask or confound war damage signals. For example, the Normalized Burn Ratio (NBR) can become less effective over time as vegetation regrowth after fires or conflict-induced damage may restore NBR values to pre-damage levels, thereby obscuring the initial impact. To overcome this limitation, a cumulative NBR as shown in Equation 1 analysis or a differencing approach over multiple time steps can be employed, enabling the capture of the entire impact trajectory and providing a more accurate assessment of damage over an extended period.

Pre-war: NBR_1

During-war: NBR_2

Post-war: NBR_3

Cumulative change: $\mathrm{NBR}_{\mathrm{cumulative}} = \sum(\mathrm{NBR}_{\mathrm{prev}} - \mathrm{NBR}_{\mathrm{current}})$

Equation 1: Claculation of cummulative dNBR

Class	**dNBR range (multiplied by 1000)**
Unburned or Regrowth	< 100
Low severity	100 - 270
Moderate low severity	270 - 440
Moderate high severity	440 - 660
High severity	>=660

Table 3 dNBR classification ranges

The classification of dNBR values as shown in Table 3 dNBR classification ranges provides a framework for interpreting the severity of changes observed in the study area, categorizing the extent of damage or recovery. These classifications range from Unburned or Regrowth (< 100), indicating areas with minimal or no visible change, to High Severity (≥ 660), representing regions with the most significant alteration.

Sentinel-2 imagery served as the primary data source for calculating the differenced Normalized Burn Ratio (dNBR) in this study. Its high temporal resolution and multispectral capabilities make it particularly suitable for monitoring changes over time, enabling detailed assessments of the spatial extent and severity of war damage. To structure the temporal analysis, a table was prepared to outline the cumulative dates used for dNBR calculations, capturing key periods such as pre-war, during-war, and post-war stages.

Date used for Pre-NBR	**Date used for Post-NBR**
27th of September 2023	1st of December 2023
1st of December 2023	20th of January 2024
20th of January 2024	12th March 2024
12th March 2024	18th June 2024
18th June 2024	13th September 2024
13th September 2024	25th November 2024

Table 4: Dates used for Pre and Post NBR

To facilitate the computation of dNBR, a custom script was developed and executed within the Google Earth Engine (GEE) platform. GEE's cloud-based environment allowed for efficient processing of large datasets, ensuring the accurate derivation of dNBR values for each specified time period. Additionally, ArcGIS Pro was employed to calculate the cumulative dNBR across the selected timeframes.

The full script used for dNBR calculation for the given data is provided in Annex 1: Google Earth Engine Script for dNBR Calculation for reference.

2.3.2 Damage Area detection using moderate resolution satellite image (Sentinel 2)

The implementation of the damage detection model involved systematic preprocessing and analysis of Sentinel-2 imagery. Training data was prepared using ArcGIS Pro's Export Training Data tool, which structured the datasets for pixel-based classification. Sentinel-2 images from three different dates were utilized to capture temporal diversity, enhancing the model's ability to generalize across varying conditions.

Preprocessing steps included atmospheric correction, cloud masking, and filtering to remove training samples affected by cloud cover. This ensured that the model learned from reliable, cloud-free data. SAMLoRA, a deep learning model for pixel classification, was used to detect damaged areas. Systematic hyperparameter tuning was performed to optimize the model's performance.

One challenge was the limited resolution of Sentinel-2 (10m), which makes detecting subtle or small-scale damage difficult. Complementary higher-resolution imagery is recommended for more detailed assessments.

The implementation of the damage detection model using moderate-resolution Sentinel-2 imagery involved several key steps, leveraging advanced DL tools and systematic hyper-parameter tuning to optimize the results.

The training data was prepared using ArcGIS Pro's DL tools, specifically the Export Training Data tool, which created structured datasets for pixel-based classification. Sentinel-2 imagery from three different dates was utilized to enhance the temporal diversity of the dataset:

One important challenge with the Sentinel-2 data is the low visual clarity of damage due to the 10m resolution. For smaller or subtle changes, higher-resolution imagery is recommended. Furthermore, cloud cover in certain regions requires careful filtering of affected training samples to prevent the model from being trained with incorrect data. This step ensures that the model only learns from reliable, cloud-free samples.

One of the significant advantages of using SAMLoRA for this task is that it does not require a pre-war image for comparison. Since SAMLoRA is capable of identifying changes based on a single post-event image, the model can directly detect damaged areas in the post-event imagery, eliminating the need for pre-war imagery. This reduces the complexity of the damage detection process and simplifies the workflow.

To enhance the model's performance and generalize better across different regions and damage types, training data for SAMLoRA is prepared using a combination of the three satellite images of different dates. This temporal diversity enriches the training dataset, ensuring that the model is exposed to a wide range of scenarios and variations in landscape conditions. By expanding the dataset in this way, SAMLoRA can learn to better distinguish between damaged and undamaged regions, improving its accuracy.

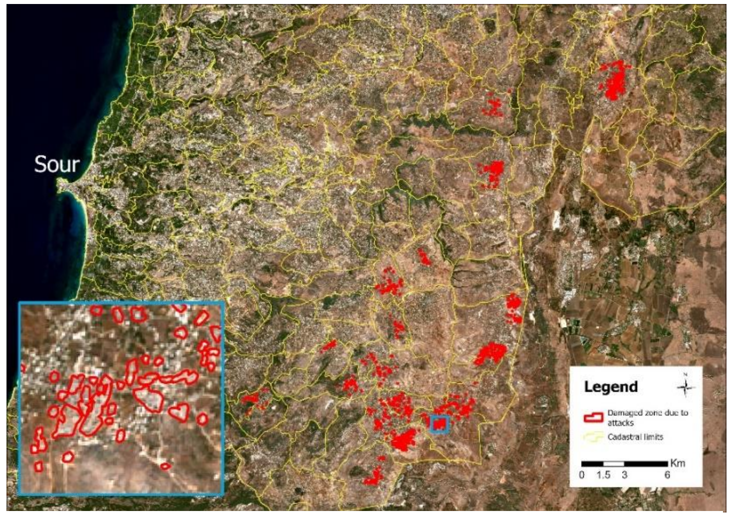

Figure 9:Map showing the damaged region at 15th November 2024

The damaged regions was digitized from various sources, including reports, news, articles, and, where available, higher-resolution satellite imagery. These sources were used to manually identify and label areas affected by Israeli violence as shown in Figure 9 .

Different combinations of Sentinel-2 spectral bands, listed in Table 5, were tested to optimize damage detection. Examples of these band combinations are shown in Figure 10.

RGB Combination (Bands 4, 3, 2)
R-NIR-SWIR Combination (Bands 4, 8, 11)
All Bands Combination
RGIR Combination (Red, Green, and Infrared)

Table 5: table showing the combination of bands used.

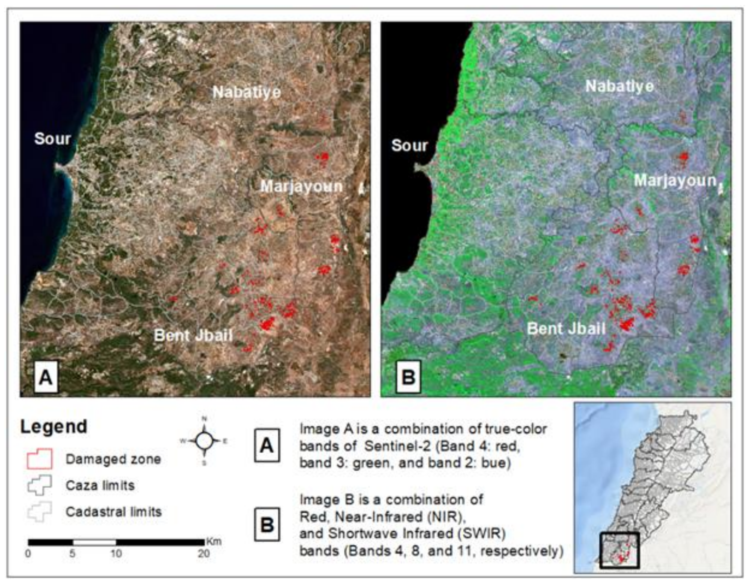

Figure 10: Images showing True-Color (Bands 4, 3, 2) and Red-NIR-SWIR (Bands 4, 8, 11) Band Combinations.

The analysis explored multiple band combinations to optimize damage detection. The **RGB Combination** (Bands 4, 3, 2) focused on true-color imagery, providing visually intuitive insights for identifying damage patterns such as debris, exposed soil, and vegetation loss. This combination was particularly effective for generating outputs that were easy to interpret by both the model and human analysts. The **R-NIR-SWIR Combination** (Bands 4, 8, 11) leveraged the spectral sensitivities of these bands to detect structural changes, vegetation stress, and soil disturbances. The inclusion of Near-Infrared (NIR) and Shortwave Infrared (SWIR) bands enhanced the model's ability to identify subtle changes that are not visible in true-color imagery. For a more comprehensive analysis, the **All-Bands Combination** utilized all available Sentinel-2 spectral bands, offering the most detailed representation of surface conditions and enabling the detection of a wide range of damage indicators. Lastly, the **RGIR Combination** (Red, Green, and Infrared) was specifically designed to target vegetation health and structural integrity, making it a focused approach for scenarios where these parameters are critical. Together, these combinations provided a robust foundation for evaluating and optimizing the damage detection process.

Following the selection of appropriate band combinations, the workflow for preparing training data involved leveraging ArcGIS Pro’s *Export Training Data* tool to ensure compatibility with the DL models being employed. The training data preparation process is critical, as the structure of the exported dataset must align with the requirements of the specific model architecture being used. Different models, such as SAMLoRA or other pixel classification frameworks, demand specific input-output structures to function optimally.

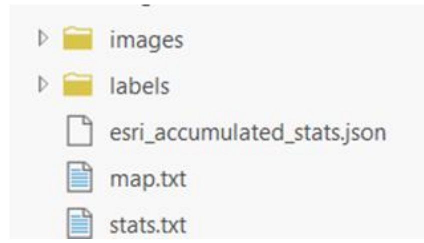

Figure 11: This screenshot displays the structure and contents of the exported training data, including imagery tiles, metadata, and label files used for AI model training.

The output dataset generated by the *Export Training Data* tool maintains a structured format, as shown in Figure 11. This structure includes two primary folders: `images` and `labels`. The `images` folder contains the input image chips, which are subsets of the larger satellite image, while the `labels` folder includes the corresponding ground truth annotations that classify regions as "damaged" or "undamaged" as shown in Figure 12. Additional files provide metadata about the training dataset, including label distribution, mapping details, and statistics, which are crucial for model setup and performance monitoring.

Different DL models may require variations in chip size, label format, or metadata to effectively process the training data. For instance, SAMLoRA requires labeled chips with precise pixel-level annotations as illustrated in Figure 12. A robust and well-structured training dataset is foundational for achieving high performance in damage detection, particularly in pixel classification tasks where precise alignment between input images and labels directly impacts the model’s learning process.

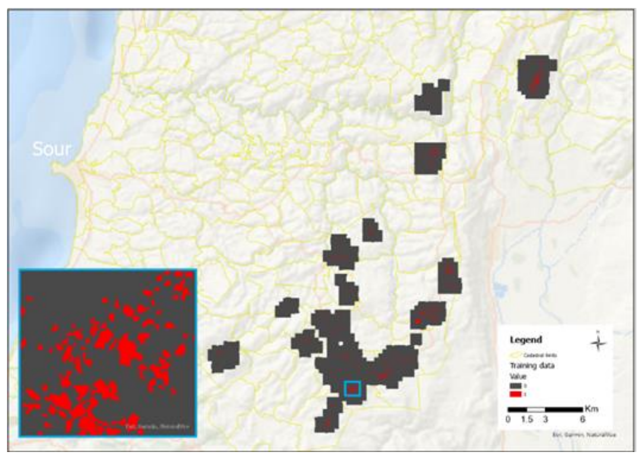

Figure 12: Map of Labeled Training Data Generated Using the Export Training Data Tool in ArcGIS Pro

The implementation of damage detection models relied on the Segment Anything Model with Low-Rank Adaptation (SAMLoRA) as the backbone for pixel classification. Two architectures, VIT_H (Vision Transformer High) and VIT_L (Vision Transformer Large), were tested to evaluate performance and scalability. Hyperparameter tuning was conducted iteratively to optimize results. Chip sizes were varied, with smaller chips (64x64) providing finer granularity and larger chips (128x128) capturing broader spatial context. A consistent batch size of 8 was used to ensure efficient training.

The script detailing this process, including the model run and performance evaluation, is provided in Annex 3: Script for Detailed Damage Detection Using Change Detector Architecture for Pixel Classification.

2.3.3 Damage building detection using high-resolution image

High-resolution satellite imagery is crucial for detecting damage at the individual building level, providing exceptional detail to identify subtle features such as roof collapses, debris patterns, and structural anomalies. With spatial resolutions ranging from 0.3 to 0.5 meters, these images allow for precise classification and identification of affected structures, making them especially valuable in densely populated or mixed-use areas.

To enable precise building-level damage detection, a comprehensive manual annotation process was conducted to classify structures as either "damaged" or "undamaged." This task required meticulous visual inspection of the high-resolution satellite imagery, identifying key indicators such as collapsed roofs, visible debris, and other structural anomalies that signify damage. Each building in the imagery was carefully evaluated, ensuring annotations accurately represented real-world conditions.

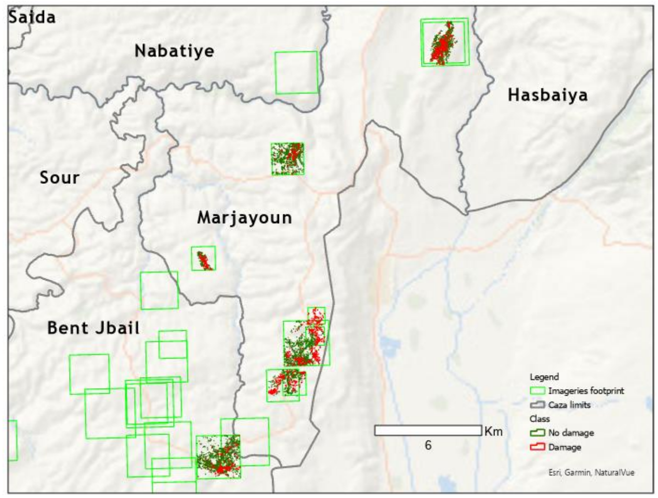

Figure 13: Map illustrating digitized building footprints, classified as either "damaged" or "undamaged."

The time-intensive process of digitizing and labeling data to prepare the training dataset is a main step in developing a robust and reliable DL model for detecting building damage. This preparation ensures the model is trained on high-quality, accurate data, forming the foundation for its effectiveness and reliability.

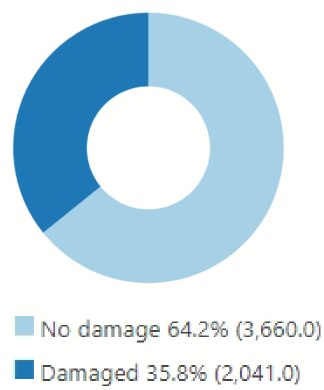

Figure 14: Pie chart showing distribution of labeled data: damaged vs. undamaged structures.

A total of 5,701 labeled annotations were created, serving as the foundation for training and evaluating the deep learning model. Among these annotations, approximately 64% were labeled as "no damage," while 36% were labeled as "damage" as shown in Figure 14. The dataset was systematically divided into two subsets: 80% for training, 20% for validation. This structured division facilitated a balanced approach, with the training subset used to teach the model, the validation subset for fine-tuning its parameters. This rigorous annotation and dataset preparation methodology was crucial in ensuring the accuracy and reliability of the machine learning model for detecting building damage.

To achieve precise building-level damage detection, the SAMLoRA model—combined with the ViT-H architecture—was selected for its advanced pixel-level classification capabilities and its capacity to capture fine-grained spatial details. By training the model on image chips of either 128x128 or 256x256 pixels, the team could systematically compare efficiency and performance to determine the optimal configuration.

Training was conducted using a Python-based TensorFlow backend. Hyperparameters, including learning rate, batch size, and chip size, were systematically tuned to achieve optimal performance. The model was evaluated using metrics such as precision, recall, and F1-score to ensure its reliability and accuracy in detecting building damage.

Hyperparameter tuning played a pivotal role in maximizing the model's performance. Parameters such as learning rate, batch size, and the number of epochs were systematically adjusted to achieve optimal results. Batch size was selected to ensure efficient utilization of computational resources while maintaining stable gradients during training. Additionally, the number of epochs was optimized to avoid overfitting, ensuring the model generalizes well to unseen data. Data augmentation techniques, such as rotation, flipping, and brightness adjustments, were also applied to enrich the training dataset and improve the model's robustness against variations in imaging conditions.

The complete script and model performance details for detecting building damage using high-resolution imagery with the SAMLoRA approach are provided in Annex 2: Script for High-Resolution Image Analysis for Building Damage Detection Using SAMLoRA.

2.3.4 Detailed damage detection using Change Detector Architecture for Pixel Classification

Change detection using DL is a process that identifies differences between two images taken at different time periods, producing a binary output that classifies each pixel as either "change" or "no change."

The Model Training and Implementation process for the Change Detector Pixel Classification Model involves using two high-resolution satellite images to identify and classify structural changes caused by conflict. These images serve as pre- and post-event data to highlight areas of damage within the study region.

Both images were georeferenced to ensure spatial alignment; however, challenges arose due to differences in their angles of view. These variations in perspective introduced inconsistencies in features such as building edges, shadows, and terrain slopes, complicating the effective detection of changes. To address these challenges, several preprocessing steps were implemented. First, both images were georeferenced to the same coordinate system, a process that involved applying transformation algorithms to achieve spatial consistency and minimize misalignment. Second, feature matching techniques, such as the Scale-Invariant Feature Transform (SIFT), were used to identify and match key feature points between the two images, further reducing distortions caused by varying viewpoints. Despite these preprocessing efforts, residual discrepancies persisted due to the inherent differences in viewing angles, which continued to pose challenges for the change detection model.

The first step in the workflow involved creating training samples by labeling areas of change and no change within the input imagery. These labeled datasets formed the foundation for training the model, enabling it to learn patterns and features that characterize changes over time. Once the labeled data was prepared, it was converted into a format suitable for deep learning, ensuring spatial alignment and proper structuring of input images and labels. The training dataset was meticulously prepared through manual digitization and labeling of buildings from pre- and post-event satellite images. This process required a detailed comparison of each building's status across the two datasets to accurately classify changes caused by Israeli aggression. A total of 5,701 buildings were labeled, with the accompanying pie chart illustrating the proportion of buildings classified as "changed" versus "no change."

The labeling process relied heavily on visual inspection and comparison of pre-event imagery (Bing Satellite, 2023) and post-event imagery (OnGeo Satellite, 2024). Key indicators of damage included visible differences in building structure, roof conditions, and surrounding debris. This rigorous labeling process ensured the preparation of a high-quality dataset, essential for training an accurate and reliable model for damage detection.

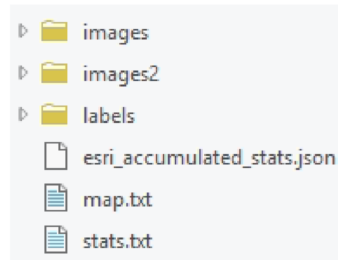

Figure 15: This screenshot displays the structure and contents of the exported training data, including two imagery tiles, metadata, and label files

After labeling the data, it was prepared in a format compatible with the Change Detection Model. Unlike standard training datasets, this preparation required three main folders: one for the labeled data (indicating "damage" and "no damage"), one for the pre-event imagery, and another for the post-event imagery. As shown in Figure 15, the dataset includes folders named "images" (pre-event imagery), "images2" (post-event imagery), and "labels" (ground truth annotations), along with metadata files such as map.txt and stats.txt. This structured format ensures the model can effectively process the temporal and spatial relationships necessary for detecting changes.

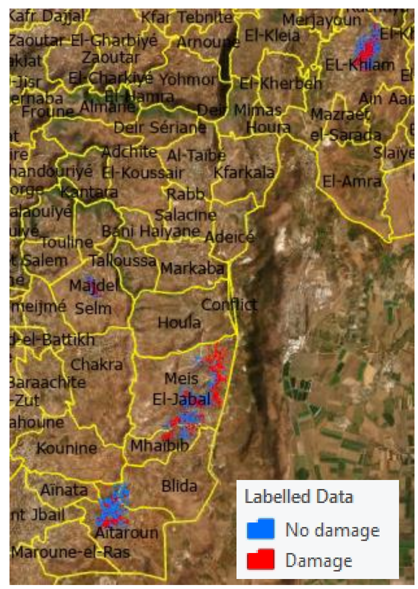

Figure 16: Map showing the digitized labeled data

The labeled data, visualized in Figure 16, highlights areas of "damage" (in red) and "no damage" (in blue) within the study area. This spatial distribution of labels across South Lebanon forms the foundation for training the model to differentiate between affected and unaffected regions. The third step, training the deep learning (DL) model, involved utilizing the prepared labeled samples to develop a model capable of detecting changes between two time periods. The model was designed to extract key features from the input images, such as spatial and spectral differences, and associate these features with the labeled classes. This process required the careful selection of an appropriate network architecture and the optimization of model parameters to achieve high accuracy in damage classification.

The training process was conducted using the ArcGIS Pro DL Framework, specifically employing the Change Detection Model to classify damage. Training data exported from ArcGIS Pro included image chips of varying sizes, such as 128x128 and 256x256 pixels, to balance the capture of fine details with broader contextual information. To enhance model performance, multiple rounds of hyperparameter tuning were undertaken, involving adjustments to critical parameters such as learning rate, batch size, number of epochs, and optimizer type. Various backbone architectures were also tested to assess their impact on feature extraction and classification accuracy.

Throughout training, validation loss was monitored to provide critical feedback, enabling the implementation of adjustments to prevent overfitting and ensure optimal generalization. The model training process began with frozen layers to stabilize feature extraction and was subsequently fine-tuned by unfreezing layers across the entire network. The labeled dataset was divided into training and validation subsets to ensure the model was exposed to diverse examples and could generalize effectively to unseen data.

The final step, detecting changes, applies the trained model to new images to generate a binary classification output. This output highlights areas where changes have occurred, providing a clear and actionable representation of differences between the two time periods. This process enables automated and accurate detection of changes at various scales, making it a valuable tool for applications requiring timely and detailed spatial analysis

2.4 Field damage assessment and monitoring

After detecting damage through remote sensing and AI-based techniques, additional detailed information is often required to provide a comprehensive understanding of the affected areas. Certain aspects, such as the extent of structural damage, number of floors, and importantly type of building, are challenging to capture either visually or through automated models. To address this limitation, a field data collection workflow was developed to gather supplementary information directly from the affected areas.

A digital form was created using **Survey123**, enabling field teams to systematically collect crucial data that cannot be inferred through imagery alone. This form includes targeted questions designed to assess damage characteristics, gather contextual information, and monitor recovery progress.

As shown in Figure 17, the form includes sections for reporting building location and additional observations.

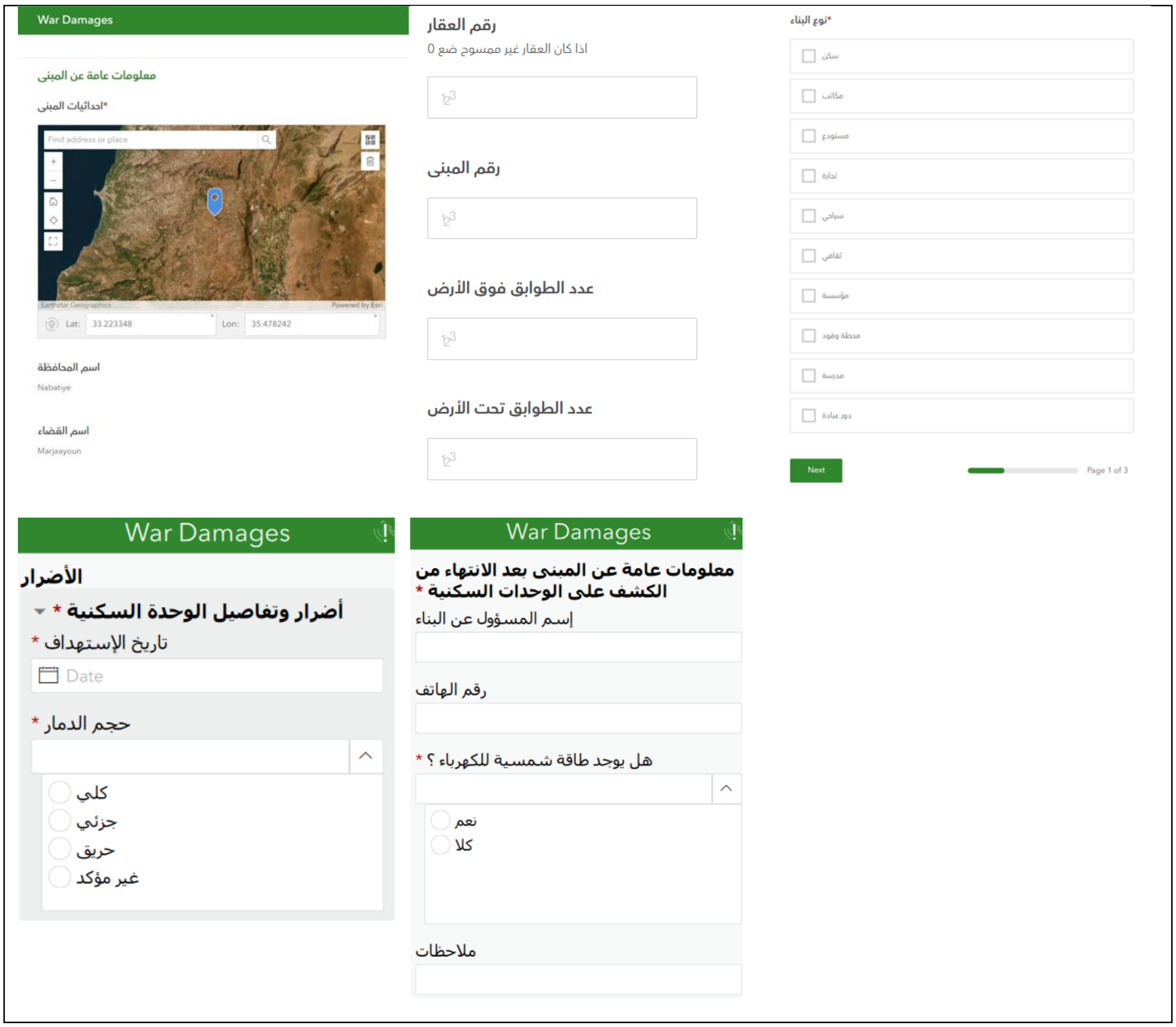

Figure 17: Overview of the customized Survey123 form designed for building damage assessment

3 Result

3.1 Evaluation of Remote Sensing Indices

The dNBR index demonstrated significant potential in distinguishing between damaged and undamaged regions within the study area. Its sensitivity to changes caused by war-related activities, proved effective in identifying areas impacted by destruction. The classification ranges applied Table 3 dNBR classification ranges allowed a clear segmentation of damage severity illustrated in Figure 18.

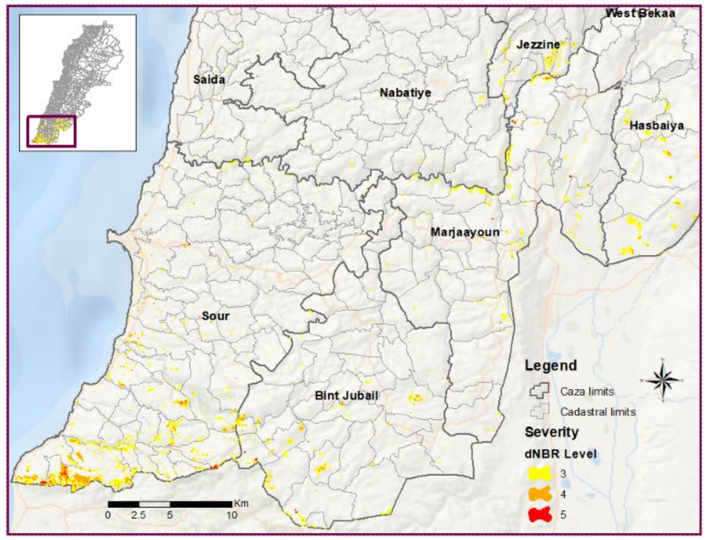

Figure 18: Map illustrating the dNBR severity classification for South Lebanon.

The dNBR calculation proved to be a highly efficient tool for preliminary damage assessments, delivering results within hours once pre- and post-event imagery was available. Its capability to utilize Sentinel-2 imagery allowed the evaluation of extensive geographic areas, making it particularly suitable for large-scale damage assessments. Additionally, the adaptability of dNBR classification ranges for severity ensured that the index could be tailored to the specific context of the study, enhancing its versatility across diverse landscapes and damage scenarios.

Mohafaza	Caza	Village	Severity level	Area (m2)
South	Sour	Aalma Ech-Chaab	Moderate	1789981.893
South	Sour	Aalma Ech-Chaab	High	968589.6607
Nabatiye	Hasbaiya	Chebaa Farms	Moderate	471888.1006
South	Sour	Borj En-Naqoura	Moderate	457678.4599

Table 6: Table highlighting regions with the maximum area under each severity level across villages in South Lebanon.

	Area (m2)			
Caza	Moderate	High	Very high	Total
Bint Jubail	1,162,031	136,416	17,722	1,316,169
Hasbaiya	792,617	86,337	499	879,453
Jezzine	405,695	26,460		432,154
Marjaayoun	826,739	70,684	20,873	918,296
Nabatiye	50,017	2,466	345	52,828
Saida	36,111	3,415	333	39,859
Sour	3,914,431	1,370,272	64,502	5,349,205
Total area of severity levels	7,187,640	1,696,049	104,275	8,987,964

Table 7: Table showing the distribution of damage severity levels (Moderate, High, and Very High) across different Cazas in South Lebanon.

The results of the cumulative dNBR analysis over one year highlight significant damage severity across South Lebanon, particularly in border regions. The Sour Caza shows the largest affected areas as shown in Table 6 , with Aalma Ech-Chaab, a border village, experiencing extensive damage. The village recorded 1,789,981 m² under moderate severity and 968,589 m² under high severity, emphasizing the aggression and violence it received due to its strategic location. Similarly, the Bint Jubail and Hasbaiya Cazas display considerable damage, with moderate severity areas exceeding 1,162,031 m² and 792,617 m², respectively.

The accompanying map visually highlights clusters of severe damage (dNBR Levels 4 and 5), concentrated in the southernmost areas, particularly around Sour and Bint Jubail, including border villages like Aalma Ech-Chaab as shown in Table 7. These findings underscore the devastating impact of the aggression on these strategically significant border regions and the urgent need for targeted recovery.

3.2 Evaluation of Damage Area detection using moderate resolution satellite image (Sentinel 2)

The evaluation of damage detection using SAMLoRA with Sentinel-2 imagery revealed notable variations in performance across different spectral band combinations, chip sizes, and model architectures. The analysis demonstrated how these factors influenced the model's ability taccurately detect damaged areas. Key metrics, including accuracy, precision, recall, and the Dice coefficient, were used to assess the model's effectiveness under different configurations.

The performance of the models was significantly influenced by the choice of spectral band combinations, with the All Bands and R-NIR-SWIR combinations consistently outperforming the RGB and RGIR combinations. This underscores the importance of leveraging spectral diversity, as a broader range of bands captures more detailed information, particularly for subtle damage indicators. Chip size also played a critical role in detection accuracy. Smaller chip sizes (64x64) generally produced better results than larger ones (128x128), likely due to their finer granularity, which enhances the detection of localized damage features. Regarding model architecture, the ViT-H backbone consistently outperformed the ViT-L backbone, particularly when processing comprehensive spectral inputs. The superior performance of ViT-H highlights its ability to capture and process complex spatial and spectral information, resulting in more precise damage classification.

The use of different band combinations was a key factor in the performance of the models, with the All Bands and R-NIR-SWIR combinations outperforming both the RGB and RGIR combinations. This underscores the significance of evaluating spectral diversity to determine which band combination yields the best results for accurate damage detection, especially in identifying subtle damage indicators. Additionally, the impact of chip size was distinguished, with smaller chip sizes (64x64) generally yielding better results than larger ones (128x128). This is likely due to the finer granularity of smaller chips, which allows for more precise detection of localized damage features. Finally, regarding model architecture, the ViT-H backbone consistently demonstrated superior performance compared to the ViT-L backbone, The VIT_H backbone demonstrates its ability to better capture and process complex information, leading to better damage classification.

The summarized findings on band combinations, chip sizes, and backbone architectures are presented in Table 8. These results provide quantitative evidence for the performance trends discussed earlier.

model name	dataset	backbone	chip size	precision	recall	f1 score
MODEL(Moderate Res -SAMLoRA) using RGB combination						
sentine64_sam_L_All	Damage_r04_bf5sept_64 Damage_r04_bf15Novt_64 Damage_r04_bf30Nov_64	VIT_L	64	0.336	0.488	0.398
sentine64pretrained_r03_sam_H_All	Damage_r04_bf5sept_64	VIT_H	64	0.35	0.52	0.419
sentine64_r03_sam_H_All	r04_nov(15 and 30)	VIT_H	64	0.327	0.453	0.379
sentine64_r02_sam_H_All	run02_all dataset	VIT_H	64	0.234	0.283	0.256
sentinel32_zone_r01_sam_H	sentinel32_OL_03	VIT_H	32	0.26	0.33	0.29
MODEL(Moderate Res -SAMLoRA) using R NIR SWIR combination						
model name	dataset	backbone	chip size	precision	recall	f1 score
sentine64_sam_H_B4_8_11_All	DS_B4B8B11_b051224 DS_B4B8B11_b151124 DS_B4B8B11_b301124	VIT_H	64	0.374	0.443	0.405
sentine64_sam_LB4_8_11_All	DS_B4B8B11_b051224 DS_B4B8B11_b151124 DS_B4B8B11_b301124	VIT_L	64	0.345	0.494	0.406
MODEL(Moderate Res -SAMLoRA) using All bands combination						
model name	dataset	backbone	chip size	precision	recall	f1 score
sentine128_vitH_AllB_DiceMonitor	DS_AllBands_301124_128 DS_AllBands_151124_128 DS_AllBands_051224_128	VIT_H	128	0.318	0.488	0.385
sentine64_vitH_AllB_Dice2	DS_AllBands_301124_64 DS_AllBands_151124_64 DS_AllBands_051224_64	VIT_H	64	0.419	0.483	0.45
MODEL(Moderate Res -SAMLoRA) using R G IR combination						
model name	dataset	backbone	chip size	precision	recall	f1 score
sent64_samlora_H	DS_64_RGIR_151124 DS_64_RGIR_301124 DS_64_RGIR_051224	Vit-H	64	0.266	0.43	0.329
sent128_samlora_H	DS_128_RGIR_151124 DS_128_RGIR_301124 DS_128_RGIR_051224	Vit-H	128	0.33	0.467	0.389

Table 8: Performance Comparison of SAMLoRA Models on High-Resolution Data

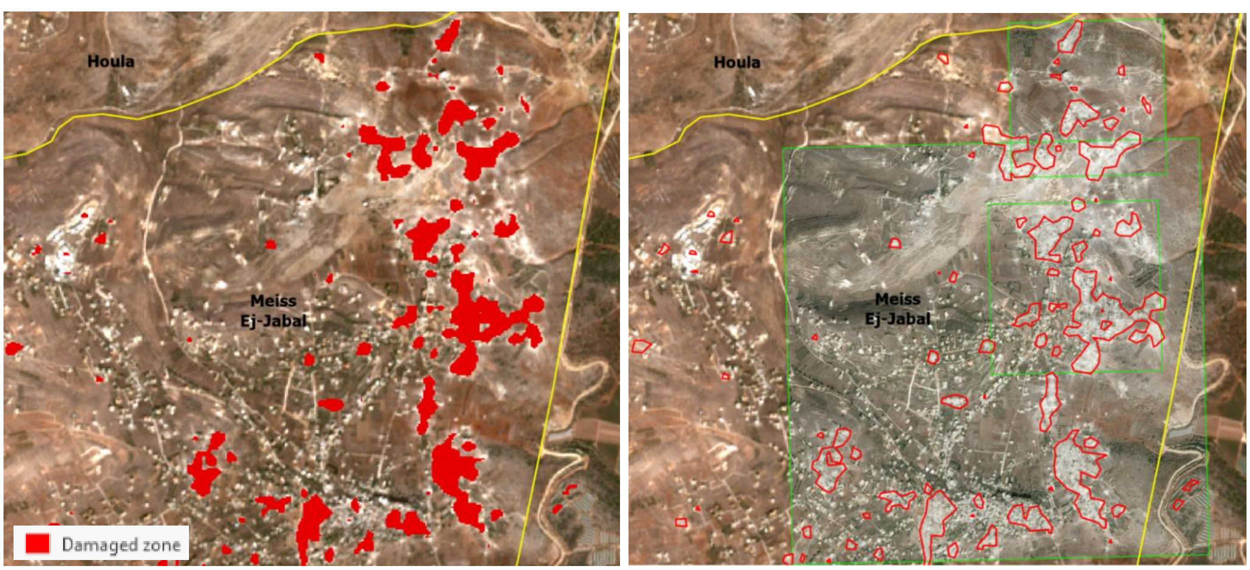

Figure 19: Predicted damaged zone using "sentine64pretrained_r03_sam_H_All" model

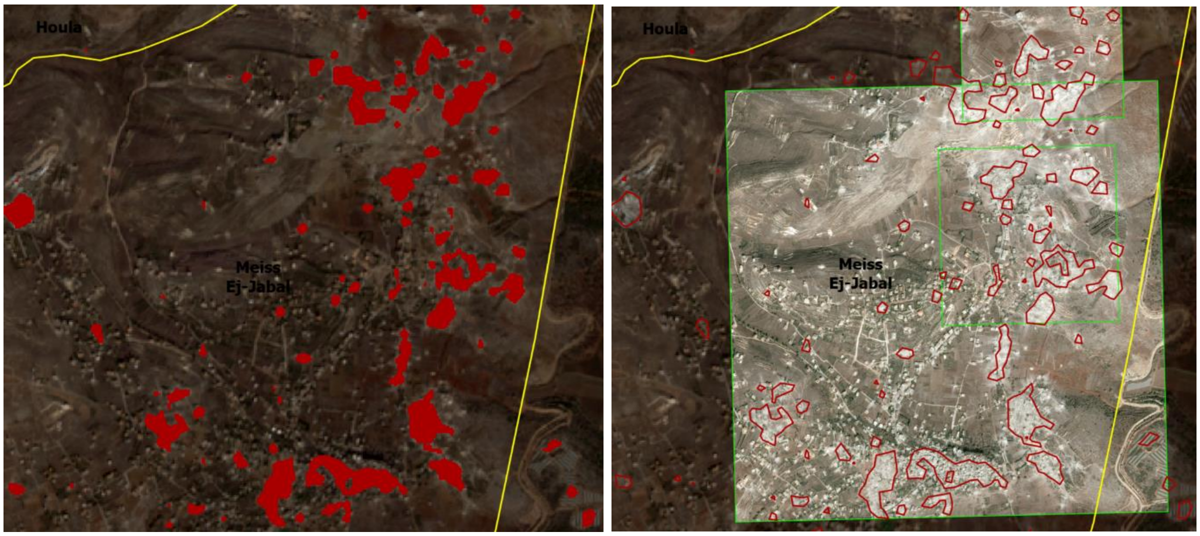

Figure 20:Predicted damaged zone using "sentine64_vitH_AllB_Dice2" model

The segmentation masks for the models with the highest precision, sentine64pretrained_r03_sam_H_All and sentine64_vitH_AllB_Dice2, demonstrate acceptable performance, exceeding initial expectations. As shown in Figure 19 (for sentine64pretrained_r03_sam_H_All) and Figure 20 (for sentine64_vitH_AllB_Dice2), both models effectively identify damaged areas. However, a notable limitation is the misclassification of a region with no actual damage, which both models incorrectly detect as damaged. This highlights the models' sensitivity to certain features in the imagery that resemble damage, underscoring the need for further refinement to enhance precision and reduce false positives. Despite these challenges, the segmentation results validate the models' potential in generating reasonably accurate damage maps, particularly for initial assessments.

As shown in Table 7, Sentinel-2 imagery provides a good starting point for damage detection, but the moderate spatial resolution limits the visual clarity of smaller damage areas. This constraint necessitates the use of higher-resolution imagery to accurately label and detect subtle structural changes. Despite these limitations, the sentine64pretrained_r03_sam_H_All model, as illustrated in Figure 19, demonstrated acceptable performance in delineating damaged areas.

Among the models, sentine64_vitH_AllB_Dice2 achieved the highest F1 score (0.45) by leveraging all Sentinel-2 bands, a 64x64 chip size, and effective class balancing. This combination utilized the full spectral diversity of the data and optimized input granularity, enabling the model to capture subtle damage features more effectively than its counterparts.

3.3 Evaluation of Building Damage Detection Using High-Resolution Satellite Imagery

The evaluation of the SAMLoRA model with the ViT-H architecture provided valuable insights into its performance for building-level damage detection. The F1-score emerged as a key metric, reflecting the harmonic mean of precision and recall. This balance accounts for both false positives and false negatives, making it particularly crucial for damage detection tasks where overestimating or underestimating damage can have significant implications for recovery efforts. A high F1-score indicates the model's ability to accurately classify damaged and undamaged buildings while minimizing errors.

High Resolution Satellite 0.3 m									
Model name	Chipsize	Backbone	Accuracy	precision		recall		F1	
				1	2	1	2	1	2
SamLora256H_1	256	VIT_H	0.9	0.72	0.53	0.705	0.659	0.714	0.5889
SamLora256H_2_cz250	256	VIT_H	0.89	0.66	0.506	0.759	0.644	0.707	0.56
SamLora128H_3	128	VIT_H	0.83	0.669	0.553	0.726	0.543	0.696	0.548

Table 9: The table presents the performance metrics of the SAMLoRA model using high-resolution satellite images.

The analysis revealed that increasing the chip size significantly enhances accuracy as shown inTable 9. Larger chip sizes provide broader spatial context, allowing the model to better understand relationships between pixels and their surroundings. This is particularly valuable in densely populated urban areas, where distinguishing between damaged and undamaged structures often requires analysing complex contextual and structural details. The improved F1-scores with larger chip sizes highlight the importance of optimizing this parameter to maximize accuracy and precision.

The training and validation loss curves for the SamLora256H_1 model, depicted in Figure 21, provide valuable insights into the model’s learning progression. The training loss (blue curve) shows a steady decline during the initial stages, reflecting the model’s ability to effectively minimize errors as it learns patterns in the data. The validation loss (orange curve) closely mirrors this trend, decreasing consistently before stabilizing, which indicates the model's ability to generalize well to unseen data.

Some minor variations in the validation loss are noticeable midway through training, possibly due to complex or ambiguous samples in the dataset. However, the overall convergence of both curves toward lower loss values demonstrates the model's stability and reliable performance. The close alignment of training and validation loss suggests that overfitting was successfully avoided, and the model achieved a balanced optimization between learning from the training data and generalizing to new inputs.

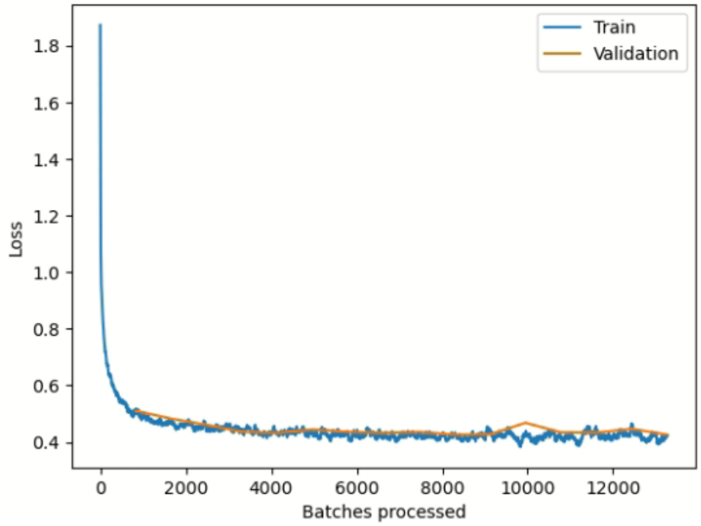

Figure 21: Training and validation loss curves throughout the model's training process for SamLora256H_1

The best-performing model configuration employed 256×256 pixel image chips, yielding the highest F1-scores for both undamaged (0.714) and damaged (0.589) buildings. In particular, the model achieved accuracy of 0.9 for identifying damaged structures—an outcome that underscores its capability to distinguish subtle signs of destruction in complex urban environments. As shown in Table 10, the training and validation loss curves drop rapidly from initially high levels and then stabilize, reflecting successful convergence and minimal overfitting. Meanwhile, the per-class metrics table confirms high accuracy in differentiating NoData areas from building footprints, with slightly lower performance in pinpointing damage severity. The additional spatial context provided by larger chip sizes appears to be the key factor in capturing both macro-level patterns (e.g., debris fields) and micro-level features (e.g., roof damage), ultimately leading to a more reliable model for building damage detection.

Analysis of the model

Per class metrics:

	NoData	1	2
precision	0.955460	0.720701	0.535171
recall	0.943164	0.714692	0.657753
f1	0.949272	0.717684	0.590164

Table 10 Performance metrics for model analysis.

While the results demonstrated the model's robustness, further improvements in precision could be achieved with a larger and more diverse training dataset. However, due to time and data constraints, expanding the dataset was not feasible for this analysis. Despite these limitations, the model performed well on unseen data, as illustrated in, which showcases the detection of damaged buildings in a previously untested area. The model's ability to generalize effectively to new regions with complex urban environments underscores its adaptability and reliability in damage detection tasks.

Figure 22 illustrates the model's ability to detect building damage on an unseen input image. The left panel shows the original high-resolution satellite imagery, while the right panel displays the model's classification results, where undamaged buildings are marked in yellow and damaged buildings in red. This visualization highlights the model's capability to generalize effectively to new areas not included in the training data, accurately identifying structural damage at the pixel level. The results demonstrate the robustness of the model, particularly in distinguishing damaged structures from their surroundings, even in complex urban environments. Such precise classifications are critical for generating actionable outputs to guide post-conflict recovery and resource allocation efforts.

<table>
<tr><th>Unseen input image</th><th>Model result</th></tr>
<tr><td>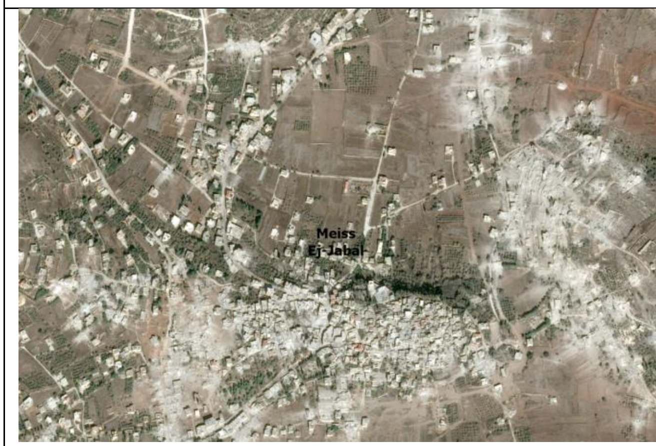
</td><td>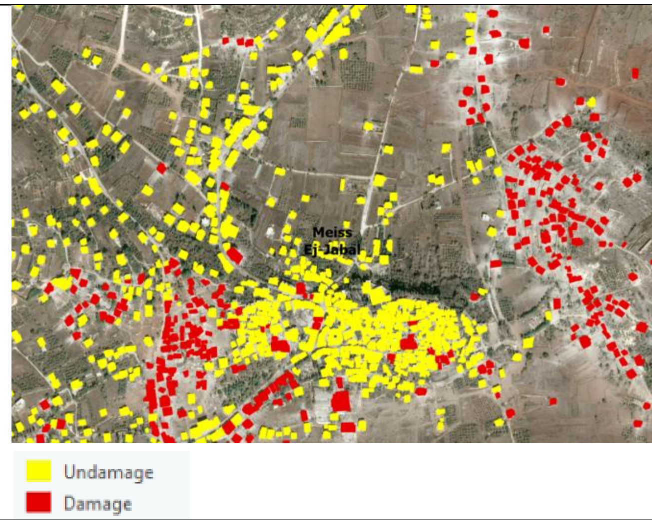
</td></tr>
</table>

Figure 22: SamLora256H_1 model performance on an unseen input image at Meis El Jabal

3.4 Evaluation of damage building detection using Change Detection Model

The performance of the Change Detection Model varied based on the backbone architecture, chip size, and training configurations, providing valuable insights into the impact of these parameters on the model's effectiveness. Among the tested backbones, ResNet101 delivered the highest precision of 0.769, demonstrating its capability to extract detailed features for accurate damage classification. However, this came at the cost of significantly longer training times. In contrast, ResNet50 showed a balance of efficiency and performance, achieving competitive results with reduced computational demand, making it a more practical choice for scalable applications.

Chip size played a crucial role in determining the model's performance, as shown in Table 11Table 11: Summary of Change Detection Model Configurations and Performance Metrics.. Models trained with smaller chip sizes (128 pixels) generally achieved higher precision by focusing on localized details. For instance, Model_Res50_DS06_r03 demonstrated notable precision (0.712), highlighting the advantages of smaller chips in capturing fine-grained damage features. However, these configurations often struggled with recall, indicating challenges in identifying all instances of damage. Conversely, larger chip sizes (256 pixels) provided a broader contextual understanding of the image, which improved the model's ability to detect damage more comprehensively. This is evident in models such as Model_Res50_DS05_r03, which achieved higher recall (0.38) despite a trade-off in precision.

model: change detection					
model name	**Backbone**	**chip size**	**precision**	**recall**	**F1**
Model_Res101_DS06_r04	RESNET101	128	0.769	0.788	0.753
Model_Res50_DS06_r03	resnet50	128	0.71229	0.22	0.29
Model_Res50_DS05_r03	resnet50	256	0.78	0.38	0.49
model_DS03_128_CD	resnet50	128	0.5995	0.337	0.38
Model_Res50_DS02_r03	resnet50	256	0.457	0.429	0.376
Model_Res50_DS02_r02	resnet50	256	0.5	0.36	0.3478
Model_Res101_DS01_r03	resnet101	256	0.346	0.241	0.205
Model_Res50_DS01_r01	resnet50	256	0.678	0.565	0.556

Table 11: Summary of Change Detection Model Configurations and Performance Metrics.

Overall, the models demonstrated the potential for automated damage detection, with *Model_Res50_DS01_r01* offering better balance of training efficiency and performance than others, achieving a precision of 0.678 and a recall of 0.565 as shown in Table 11. Figure 23 illustrates the training and validation loss curves during the training process for this model. The steady decline in the training loss (blue curve) demonstrates the model's ability to effectively learn from the training data by adjusting its internal parameters to minimize errors. Meanwhile, the consistent decline in the validation loss (orange curve) during the initial training stages highlights the model's capacity to generalize to unseen data. As training progresses, the stabilization of the validation loss suggests that the model has reached optimal performance under the current configuration. The absence of a sharp increase in validation loss further indicates minimal overfitting, showcasing a balanced and robust training process. This graph provides key insights into the model's learning dynamics, even as its final performance metrics surpass what is implied by the loss curves.

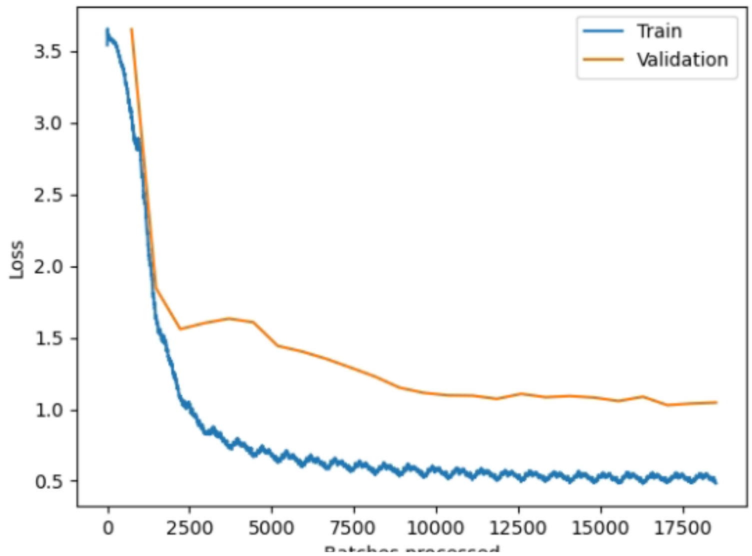

Figure 23: Training and validation loss curves across the number of processed batches for model Model_Res50_DS01_r01.

Despite these promising results, some challenges persisted. The varying angles of view between the pre- and post-event images impacted the alignment of features, which in turn affected recall, particularly for smaller or subtle damages. The experimentation revealed that larger chip sizes and longer training times could partially mitigate these issues.

The evaluation of these models on unseen data demonstrates their potential for real-world applications but also reveals certain limitations, such as detecting changes unrelated to damage. Both models exhibited moderate scalability, performing reasonably well across diverse regions, which suggests they could be applied to large-scale damage detection tasks. However, their performance may vary depending on the complexity of the landscape. Among the models, Model_Res50_DS01_r01 stands out for its better detection capabilities, particularly in identifying structural changes. Nevertheless, as shown in Figure 24, the segmentation masks produced by the models reveal both strengths and weaknesses. While the models successfully identified many areas of structural change, inaccuracies such as false positives (non-damage changes incorrectly flagged as damage) and missed detections (damaged areas not identified) were observed. These issues underscore the need for further optimization to improve precision and recall, thereby enhancing the reliability of the models in damage assessment tasks.

Images pre- war and post war **Model run result**

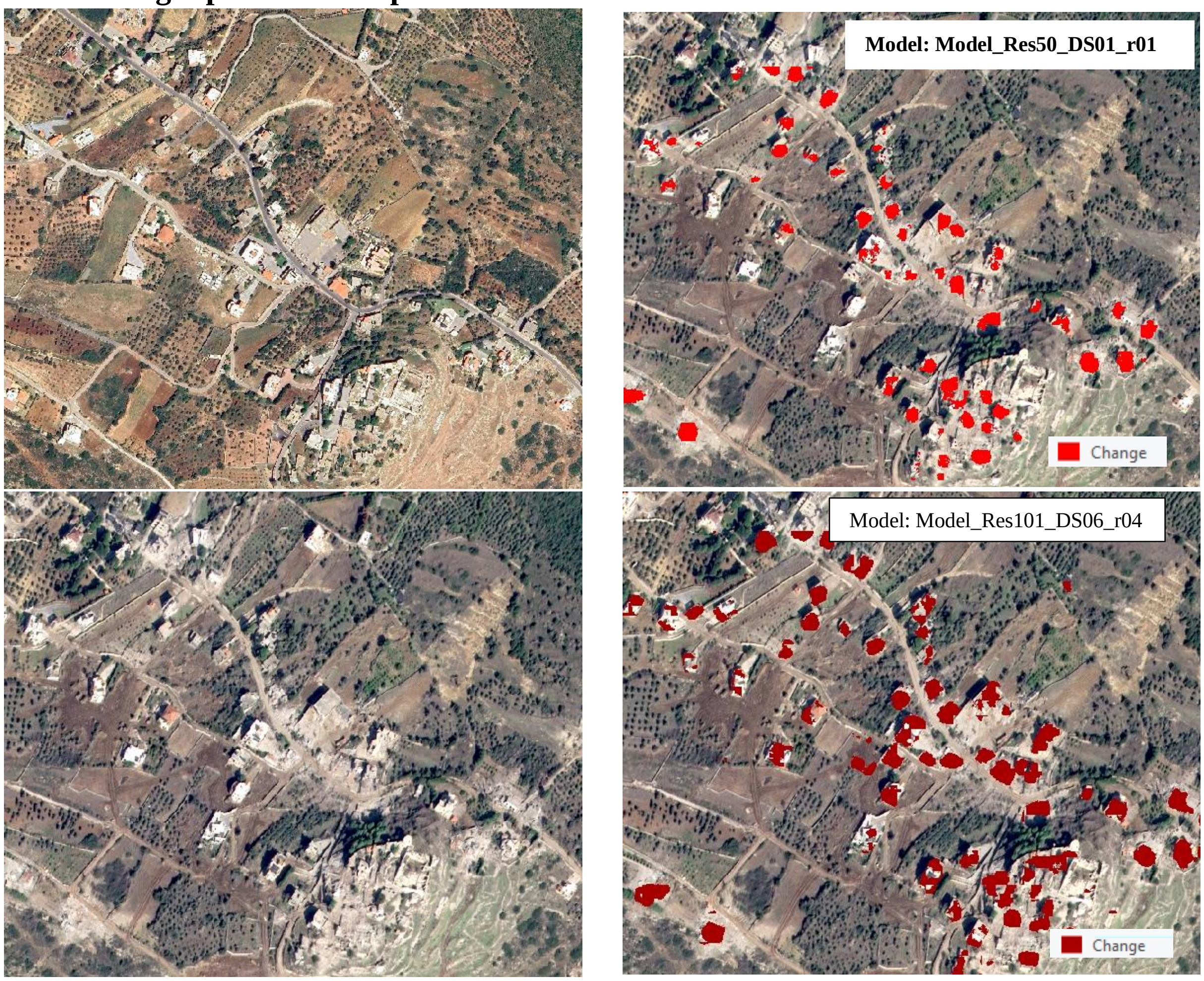

Figure 24:Pre-war and post-war satellite imagery (left column), with model-derived damage detection outputs (right column). Red polygons indicate areas identified as having undergone significant structural changes, highlighting the model's ability to pinpoint damaged buildings in the post-war landscape

In conclusion, the Change Detection Model trained with ResNet50 and a chip size of 256 pixels emerged as a relatively efficient configuration, balancing performance with manageable training times. While its results may not be fully reliable in complex scenarios, this approach supports timely damage assessment, providing a preliminary tool for decision-making in post-war reconstruction and aid distribution. The segmentation masks in Figure 24 demonstrate the ability of both models to detect damaged structures, although the accuracy varies depending on the region and complexity of the landscape.

3.5 Monitoring of field damage survey

Due to safety concerns in South Lebanon, conducting field surveys was not feasible. However, this section outlines the workflow designed to facilitate effective data collection and monitoring if field visits were possible. The proposed system integrates real-time synchronization and visualization of field data through ArcGIS Online, ensuring efficient survey management and data analysis.

The synchronized entries were automatically displayed on an interactive dashboard, which served as a centralized platform for monitoring survey progress and analyzing results. A screenshot of this dashboard is shown below, illustrating its capabilities and workflow design.

The dashboard offered several key functionalities to streamline the monitoring and analysis of field data as shown in the Figure 25. Geospatial visualization displayed georeferenced field data on an interactive map, illustrating the spatial distribution of damaged buildings across the study area. Damage categorization provided graphical summaries of damage levels (e.g., minor, moderate, severe), offering insights into the extent of destruction. Progress monitoring enabled real-time tracking of survey progress, including the number of buildings assessed ensuring effective management of data collection activities. Additionally, synchronized data entries triggered automatic updates to maps, charts, and statistics, ensuring access to the most up-to-date information.

Figure 25: Interactive Esri Dashboard showcasing geospatial insights: visualizing real-time data on building damage, survey progress, and spatial distribution through dynamic maps and charts

4 Discussion

This chapter presents the analysis of the results obtained from the methodologies applied in this study. The findings are interpreted in the context of their implications, limitations, and potential for future advancements.

4.1 Remote Sensing Indices findings

The application of dNBR for damage assessment demonstrated its capability to rapidly and efficiently identify large-scale destruction. Using Sentinel-2 imagery, the index successfully detected significant damage patterns across South Lebanon, particularly in border regions such as Aalma Ech-Chaab and Bint Jubail. However, its reliance on medium-resolution imagery restricts its effectiveness in detecting finer details, especially in densely populated areas with smaller-scale damage.

4.2 Moderate-Resolution Satellite imagery for damage detection model performance

The SAMLoRA model applied to Sentinel-2 imagery demonstrated performance variations based on spectral band combinations, chip sizes, and model architecture. The use of All Bands and RGB combinations proved effective in detecting damage, emphasizing the importance of spectral diversity in identifying subtle damage indicators. Smaller chip sizes (64x64) with ViT-H backbone were more effective at capturing localized damage features but required higher computational resources.

However, due to the medium resolution of Sentinel-2 imagery, the model is limited to detecting damage at the zone level rather than the building level. The segmentation masks produced by the two models at the same region, Houla and Meis El Jabal, showed good precision, with approximately 80% of the detected areas being accurately classified as damaged, and while 20% were false detections. Both images identified the same regions as damaged, though with slight variations in the extent of the affected areas.

4.3 Building-Level Damage Detection Using High-Resolution Imagery

The integration of high-resolution imagery with the SAMLoRA model enabled detailed detection of building-level damage, achieving an impressive 0.9 accuracy in identifying damaged structures, particularly in complex urban environments. The 256x256 chip size configuration provided sufficient spatial context for accurate structural damage detection.

However, several limitations were identified. False positives and missed detections arose mainly due to the limited diversity of the training dataset, hindering the model's generalization across varied scenarios. In densely built areas, the model accurately classified buildings as damaged or undamaged but struggled to delineate closely spaced structures, often grouping them as a single entity.

Testing in regions such as Houla and Meis El Jabal demonstrated the model's ability to classify damaged buildings with high accuracy, though the challenge of delineating adjacent structures remained. Enhancing the training dataset and refining the model architecture are crucial for improving segmentation precision, especially in densely built environments.

4.4 Change Detection Model for Damage Assessment

The Change Detection Model, particularly configurations using ResNet50 and 256-pixel chips, demonstrated a balanced performance in terms of precision and recall. The results underscore the importance of contextual information in detecting structural changes. However, the model's performance was influenced by challenges such as misalignment between pre- and post-event imagery and false positives related to non-damage changes.

While the Change Detection Model offers potential for real-world applications, further improvements are needed to enhance its scalability and reliability. Future work could focus on optimizing feature alignment techniques and incorporating additional pre-processing steps to mitigate alignment challenges.

Conclusion and Perspectives

This study presented an integrated approach for war damage assessment in South Lebanon, combining remote sensing indices, AI-based methodologies, and satellite imagery of varying resolutions. The dNBR index proved to be a practical tool for preliminary damage assessments, enabling the rapid identification of affected areas across large geographic extents.

The SAMLoRA model was applied to both moderate- and high-resolution imagery. Moderate-resolution imagery facilitated faster detection of damage zones, serving as an accessible and cost-effective solution until higher-resolution images became available. High-resolution imagery enabled detailed building-level damage detection. However, challenges such as difficulties in delineating closely spaced buildings and reliance on a limited training dataset were noted. Addressing these issues will require further refinement of model architectures and the inclusion of more diverse training data.

When using the change detection model, acquiring pre- and post-war images from the same satellite and within the same season is essential to minimize variations caused by differences in viewing angles and shadows. While this approach increases costs due to the need for multiple acquisitions, the SAMLoRA model requires only post-war imagery, making it a more economical option for detailed damage assessments in resource-constrained contexts.

Future work should focus on integrating field surveys with AI-based damage assessments. Field surveys provide critical ground-truth data for validating detected damage, bridging the gap between automated assessments and on-the-ground realities. A survey has already been developed to systematically collect detailed information, but it requires completion to ensure comprehensive coverage of affected areas.

The existing dashboard is designed to display real-time updates from the field survey, providing a clear view of completed and pending assessments. This interactive platform enables decision-makers to analyze data through tables and maps, facilitating informed decisions. Overlaying the results of damaged buildings detected by the SAMLoRA model with field survey data allows for robust validation, identifying areas of agreement and discrepancies.

This integration will significantly enhance the accuracy of damage assessments and provide stakeholders with essential insights into the type and severity of damage. Such insights enable the prioritization of recovery efforts, guiding decision-makers on where to begin interventions and ensuring efficient resource allocation for a streamlined recovery process.

References

Adegun, Adekanmi Adeyinka, Serestina Viriri, and Jules-Raymond Tapamo. "Review of Deep Learning Methods for Remote Sensing Satellite Images Classification: Experimental Survey and Comparative Analysis." *Journal of Big Data* 10, no. 1 (2023).

Ahmad, Rami. "Smart Remote Sensing Network for Disaster Management: An Overview." *Telecommunication Systems* 87 (2024): 213-237.

Aimaiti, Yusupujiang, Christina Sanon, Magaly Koch, Laurie G.. Baise, and Babak Moaveni. "War Related Building Damage Assessment in Kyiv, Ukraine,Using Sentinel-1 Radar and Sentinel-2 Optical Images." *Remote Sensing* 14 (December 2022).

Al Shafian, Sultan, and Da Hu. "Integrating Machine Learning and Remote Sensing in Disaster Management: A Decadal Review of Post-Disaster Building Damage Assessment." *MDPI* 14, no. 8 (July 2024).

Ali Eli, Aimina, and Abida Ali. "Deep Learning Applications in Medical Image Analysis: Advancements, Challenges, and Future Directions." *arXiv*, 2024.

Bai, Yongsheng, Bing Zha, Halil Sezen, and Alper. Yilmaz. "Engineering deep learning methods on automatic detection of damage in infrastructure due to extreme events." *Structural Health Monitoring* 22, no. 59 (2022).

Bashir Khajwal, Asim, Chih-Shen Cheng, and Arash Noshadravan. "Multi-view deep learning for reliable post-disaster damage classification." *arXiv*, August 2022.

Campbell, James B., and Randolph H. Wynne. "History and scope of remote sensing." In *Introduction to Remote Sensing, Fifth Edition.* . 2011.

Chen, Tao, Zhiyuan Lu, Yue Yang, and Yuxiang Zhang. "A Siamese Network Based U-Net for Change Detection in High Resolution Remote Sensing Images." *IEEE Journal of Selected Topics in Applied Earth Observations and Remote Sensing* 15, no. 1 (n.d.).

Forsyth, David, and Jean Ponce. *Computer vision: a modern approach.* ACM Digital Library, 2002.

Garcia-Garcia, Alberto, Sergio Orts-Escolano, Sergiu Oprea, Victor Villena-Martinez, and Jose Garcia-Rodriguez. "A Review on Deep Learning Techniques Applied to Semantic Segmentation." *arXiv* 1 (2017).

Geography, What is Remote Sensing? The Definitive Guide - GIS. *GIS Geography.* 2024. https://gisgeography.com/remote-sensing-earth-observation-guide/.

Girshick, Ross, Jeff Donahue, Trevor Darrell, and Jitendra Malik. "Rich Feature Hierarchies for Accurate Object Detection and Semantic Segmentation." *IEEE Transactions on Pattern Analysis and Machine Intelligence (TPAMI)*, 2014.

Holail, Shimaa, et al. "Time-series satellite remote sensing reveals gradually increasing war damage in the Gaza Strip." *National Science Review* 11, no. 9 (September 2024).

INTERSOS. *The Impact of War on Infrastructure: South Lebanon as a Case Study.* 2024.

Jamil, Akhtar and Khan, Aftab, Bulent Bayram, Javed Iqbal, Gomal Amin, Mirsat Yesiltepe, and Dostdar Hussain. "SPATIO-TEMPORAL GLACIER CHANGE DETECTION USING DEEP LEARNING: A CASE STUDY OF SHISHPER GLACIER IN HUNZA." *International Symposium on Applied Geoinformatics* 11 (2019).

Joyce, Karen E., Kim C. Wright, Sergey V. Samsonov, and Vincent G. Ambrosia. "Remote sensing and the disaster management cycle." *Intechopen*, 2024.

Kaur, Jaskirat, and Williamjeet Singh. "Tools, Techniques, Datasets and Application Areas for Object Detection in an Image: A Review." *Multimedia Tools and Applications* 81 (2022).

Key, Carl H, Nathan C Benson, and others. "Landscape assessment (LA)." *FIREMON: Fire effects monitoring and inventory system* (US Department of Agriculture, Forest Service, Rocky Mountain Research), 2006: 164.

LeCun, Yann, Yoshua Bengio, and Geoffrey Hinton. "Deep learning." *Nature* (Nature Publishing Group UK London) 521, no. 7553 (2015): 436--444.

Lillesand, Thomas M., Ralph W. Kiefer, and Jonathan W. Chipman. "REMOTESENSING AND IMAGE INTERPRETATION Seventh Edition." 2015.

Liu, Tao, Lexie Yang, and Dalton Lunga. "Change detection using deep learning approach with object-based image analysis." *Remote Sensing of Environment* 256 (2021).

Lv, Jinna, Qi Shen, Mingzheng Lv, Yiran Li, and Lei Shi. "Deep learning-based semantic segmentation of remote sensing images: a review." *Frontiers in Ecology and Evolution* 11 (July 2023).

Ma, Lei, Yu Liu, Xueliang Zhang, Yuanxin Ye, Gaofei Yin, and Brian Alan Johnson. "Deep learning in remote sensing applications: A meta-analysis and review." *ISPRS journal of photogrammetry and remote sensing* (Elsevier), 2019: 166--177.

MacQueen, Benjamin. "Continuity, Change, Conflict and Co-operation." In *An Introduction to Middle East Politics*, 73. Sage Publishing, 2013.

MathWorks. 2024. https://www.mathworks.com/discovery/object-detection.html.

Mitchell, Tom. *Machine learning.* Vol. 1. 9 vols. New York: McGraw-hill, 1997.

Planitz, Angelika. "A Guide To Successful Damage And Needs Assessment." *ALNAP*, 1997.

Prado Osco, Lucas, et al. "The Segment Anything Model (SAM) for Remote Sensing Applications: From Zero to One Shot." *arXiv* 2 (2023).

Qiao, HJ, X Wan, J Zh Xu, Sh Y Li, and PP}, He. "Deep learning based optical flow estimation for change detection: A case study in Indonesia earthquake." *ISPRS* (Copernicus Publications) 3 (2020): 317--322.

Ren, Shaoqing, Kaiming He, Ross Girshick, and Jian Sun. "Faster R-CNN: Towards real-time object detection with region proposal networks." *IEEE transactions on pattern analysis and machine intelligence* (IEEE) 39, no. 6 (2016): 1137--1149.

Richards, John A. *Remote sensing digital image analysis.* Vol. 5. Springer, 2022.

Richards, John A. "Sources and Characteristics of Remote Sensing Image Data." In *Remote Sensing Digital Image Analysis*, 1-19. 2022.

Risso, Matteo, et al. "Building Damage Assessment in Conflict Zones: A Deep Learning Approach Using Geospatial Sub-Meter Resolution Data." *International Conference on ImageProcessing Applications and Systems*, October 2024.

Ronneberger, Olaf, Philipp Fischer, and Thomas Brox. "U-net: Convolutional networks for biomedical image segmentation." In *Medical image computing and computer-assisted intervention*, 234--241. Munich, 2015.

Russell, Stuart J, and Peter Norvig. *Artificial intelligence: a modern approach.* 4th. Pearson, 2021.

Samuel, A. L. "Some Studies in Machine Learning Using the Game of Checkers." (IBM) 3, no. 3 (1959): 210 - 229.

Shorten, Connor, and Taghi M. Khoshgoftaar. "A survey on Image Data Augmentation for Deep Learning." *Journal of Big Data* 6, no. 1 (2019).

Voigt, Stefan, Thomas Kemper, Torsten Riedlinger, Ralph Kiefl, Klaas Scholte, and Harald Mehl. "Satellite Image Analysis for Disaster and Crisis-Management Support." *ieeexplore* 45, no. 6 (2007): 1520 - 1528.

Wang, Di, et al. "SAMRS: Scaling-up Remote Sensing Segmentation Dataset with Segment Anything Model." *arVix*, 2023.

Weinthal, Erika. "Earlier Assessments of Conflict Damage Can Spur Timely Relief." *New Security Beat*, 2024.

Xia, Haobin, et al. "A Deep Learning Application for Building Damage Assessment Using Ultra-High-Resolution Remote Sensing Imagery in Turkey Earthquake." *Int J Disaster Risk Sci* 14 (2023).

Xu, Hanqiu. "Extraction of urban built-up land features from Landsat imagery using a thematicoriented index combination technique." *Photogrammetric Engineering \& Remote Sensing* (American Society for Photogrammetry and Remote Sensing) 73, no. 12 (2007): 1381--1391.

Xu, Joseph Z., Wenhan Lu, Li, Zebo Khaitan, Pranav, and Valeriya Zaytseva. "Building Damage Detection in Satellite Imagery Using Convolutional Neural Networks." *arXiv*, October 2019.

Xu, Joseph, and Pranav Khaitan. "Machine Learning-based Damage Assessment for Disaster Relief." *Google Research Blog.* 2020. https://research.google/blog/machine-learning-based-damage-assessment-for-disaster-relief/.

Z. Xu, Joseph, Wenhan Lu, Zebo Li, Pranav Khaitan, and Zaytseva Valeriya. "Networks, Building Damage Detection in Satellite Imagery Using Convolutional Neural." *Remote Sensing of Environment*, 2021.

Zha, Yong, Jay Gao, and Shaoxiang Ni. "Use of normalized difference built-up index in automatically mapping urban areas from TM imagery." *International journal of remote sensing* (Taylor & Francis) 24, no. 3 (2003): 583--594.

Zhang, Hua, Zhengang Jiang, Guoxun Zheng, and Xuekun Yao. "Semantic Segmentation of High-Resolution Remote Sensing Images with Improved U-Net Based on Transfer Learning." *International Journal of Computational Intelligence Systems* (Springer) 16, no. 181 (2023).

Zheng, Zhuo, Yanfei Zhong, Junjue Wang, Ailong Ma, and Liangpei Zhang. "Building damage assessment for rapid disaster response with a deep object-based semantic change detection framework: From natural disasters to man-made disasters." *Remote Sensing of Environment* 265 (2021).

Zhu, Xiao Xiang and Tuia, Devis, Lichao Mou, Gui-Song Xia, Liangpei Zhang, Feng Xu, and Friedrich Fraundorfer. "Deep learning in remote sensing: A comprehensive review and list of resources." *IEEE geoscience and remote sensing magazine* (IEEE) 5, no. 4 (2017): 8--36.

Appendix

Annex 1: Google Earth Engine Script for dNBR Calculation for reference.

Annex 2: Script for High-Resolution Image Analysis for Building Damage Detection Using SAMLoRA

Annex 3: Script for Detailed Damage Detection Using Change Detector Architecture for Pixel Classification.

5 Annex A: Google Earth Engine Script for dNBR Calculation

The script below demonstrates the implementation of dNBR calculation in Google Earth Engine using Sentinel-2 imagery:

```
//////////////////////////////////////////////////////////////////////////////////////////////////////////
//Define the study area (geometry)
   ee.Geometry.Polygon(
      [[[35.090020185800135, 33.43729543835547],
        [35.090020185800135, 33.04908565344313],
        [35.894768720956385, 33.04908565344313],
        [35.894768720956385, 33.43729543835547]]], null, false);


// Define DNBR intervals
var unburned = [-0.1, 0.1];
var lowSeverity = [0.1, 0.27];
var moderatelowSeverity = [0.27, 0.44];
var moderateHighSeverity = [0.44, 0.66];
var highSeverity = [0.66, 1.3];

// Load Sentinel-2 image collection
var collection1 = ee.ImageCollection('COPERNICUS/S2_SR')
  .filterDate('yyyy-mm-dd', 'yyyy-mm-dd')
  .filterBounds(geometry)
  .filterMetadata('CLOUDY_PIXEL_PERCENTAGE', 'less_than', 60);

var collection2 = ee.ImageCollection('COPERNICUS/S2_SR')
  .filterDate('yyyy-mm-dd', 'yyyy-mm-dd') // range of date
  .filterBounds(geometry)
  .filterMetadata('CLOUDY_PIXEL_PERCENTAGE', 'less_than', 60);

// Calculate DNBR
var preFireImage = ee.Image(collection1.median())
  .select(['B8', 'B12'])  // NIR and SWIR bands
  .divide(10000);  // Scale the reflectance values

var postFireImage = ee.Image(collection2.median())
  .select(['B8', 'B12'])  // NIR and SWIR bands
  .divide(10000);  // Scale the reflectance values

var nbr1 = preFireImage.normalizedDifference(['B8', 'B12'])
  .rename('NBR1');

var nbr2 = postFireImage.normalizedDifference(['B8', 'B12'])
  .rename('NBR2');
```

```
var dnbrImage = nbr1.subtract(nbr2); // Calculate DNBR

// Create a function to classify DNBR into severity intervals
var classifyDNBR = function(image) {
  var classifiedImage = ee.Image(0); // Initialize an empty image

  // Apply the severity intervals using conditional statements
  classifiedImage = classifiedImage.where(
    image.gt(unburned[0]).and(image.lte(unburned[1])), 1); // Unburned
  classifiedImage = classifiedImage.where(
    image.gt(lowSeverity[0]).and(image.lte(lowSeverity[1])), 2); // Low Severity
  classifiedImage = classifiedImage.where(
    image.gt(moderatelowSeverity[0]).and(image.lte(moderatelowSeverity[1])), 3); // Moderate
Low Severity
  classifiedImage = classifiedImage.where(
    image.gt(moderateHighSeverity[0]).and(image.lte(moderateHighSeverity[1])), 4); // Moderate
High Severity
  classifiedImage = classifiedImage.where(
    image.gt(highSeverity[0]).and(image.lte(highSeverity[1])), 5); // High Severity

  // Mask areas outside the defined severity intervals
  classifiedImage = classifiedImage.selfMask();

  return classifiedImage;
};

// Apply the DNBR classification to the image
var classifiedDNBR = classifyDNBR(dnbrImage);

// Visualization parameters for the severity intervals
var visParams = {
  min: 1,
  max: 4,
  palette: ['green', 'yellow', 'orange', 'red','magenta']
};

// Export the classified DNBR image if needed
Export.image.toDrive({
  image: dnbrImage.clip(geometry),
  description: 'DNBR_month',
  folder: 'MasterProject', // Replace with your desired folder name in Google Drive
  scale: 20, // Replace with the desired scale (resolution) in meters
  region: geometry,

});
```

Annex 2: Script for High-Resolution Image Analysis for Building Damage Detection Using SAMLoRA

```
################Export Training Dataset###################
  arcpy.ia.ExportTrainingDataForDeepLearning(
   in_raster="HR_Mosaic_03m_R02.tif",
   out_folder=r"E:\Detect_Damage_Samah\PixelClassification\Dataset_256",
   in_class_data="TOtalDamage1_filtered1",
   image_chip_format="TIFF",
   tile_size_x=256,
   tile_size_y=256,
   stride_x=128,
   stride_y=128,
   output_nofeature_tiles="ONLY_TILES_WITH_FEATURES",
   metadata_format="Classified_Tiles",
   start_index=0,
   class_value_field="class_Nov",
   buffer_radius=0,
   in_mask_polygons=None,
   rotation_angle=0,
   reference_system="MAP_SPACE",
   processing_mode="PROCESS_AS_MOSAICKED_IMAGE",
   blacken_around_feature="NO_BLACKEN",
   crop_mode="FIXED_SIZE",
   in_raster2=None,
   in_instance_data=None,
   instance_class_value_field=None,
   min_polygon_overlap_ratio=0
)



###Final Training model###########################
with arcpy.EnvManager(gpuId=1):
with arcpy.EnvManager(gpuId=1):
   arcpy.ia.TrainDeepLearningModel(
      in_folder=r"E:\Detect_Damage_Samah\PixelClassification\Dataset_256",
      out_folder=r"E:\Detect_Damage_Samah\PixelClassification\Models\SamLora256H_1",
      max_epochs=100,
      model_type="SAMLORA",
      batch_size=8,
      arguments="class_balancing False;ignore_classes #",
      learning_rate=None,
      backbone_model="VIT_H",
      pretrained_model=None,
```

```
        validation_percentage=20,
        stop_training="STOP_TRAINING",
        freeze="UNFREEZE_MODEL",
        augmentation="CUSTOM",
        augmentation_parameters="rotate '30.0;0.5';brightness '(0.4,0.6);1.0';contrast
'(0.75,1.5);1.0';zoom '(1.0,1.2);1.0';crop '224;1.0;(0,1);(0,1)'",
        chip_size=256,
        resize_to="",
        weight_init_scheme="",
        monitor="VALID_LOSS"
    )
```

Model run for final model:

Train Deep Learning Model
=====================
Tool Path

Input Training Data   E:\Detect_Damage_Samah\PixelClassification\Dataset_256
Output Folder   E:\Detect_Damage_Samah\PixelClassification\Models\SamLora256H_1
Max Epochs   100
Model Type   SAMLORA
Batch Size   8
Model Arguments   class_balancing False;ignore_classes #
Learning Rate
Backbone Model   VIT_H
Pre-trained Model
Validation %   20
Stop when model stops improving   STOP_TRAINING
Output Model
E:\Detect_Damage_Samah\PixelClassification\Models\SamLora256H_1\SamLora256H_1.dlpk
Freeze Model   UNFREEZE_MODEL
Data Augmentation   CUSTOM
Augmentation Parameters   rotate '30.0;0.5';brightness '(0.4,0.6);1.0';contrast
'(0.75,1.5);1.0';zoom '(1.0,1.2);1.0';crop '224;1.0;(0,1);(0,1)'
Chip Size   256
Resize To
Weight Initialization Scheme
Monitor Metric   VALID_LOSS
=====================
Environments

GPU ID   1
=====================
Messages

Start Time: Friday, December 13, 2024 10:26:23 PM
Learning Rate - 0.00010964781961431851

epoch	training loss	validation loss	accuracy	Dice	time
0	0.5034894347190857	0.5109672546386719	0.8912842869758606	0.5098706483840942	00:28:46
1	0.4728110730648041	0.48285970091819763	0.8853575587272644	0.5254727602005005	00:28:26
2	0.44193655252456665	0.4608607590198517	0.8910240530967712	0.5437813997268677	00:28:28
3	0.4400990903377533	0.43645361065864563	0.8952534198760986	0.5646746158599854	00:32:53
4	0.4324365258216858	0.43263739347457886	0.8990359306335449	0.5674175024032593	00:28:33
5	0.4310499131679535	0.4446924924850464	0.9039262533187866	0.5602661967277527	01:21:58
6	0.4238850772380829	0.4365260899066925	0.9029025435447693	0.5596798062324524	04:32:07
7	0.4172075390815735	0.4326550364494324	0.9064227938652039	0.565973162651062	04:47:01
8	0.42410677671432495	0.4359246790409088	0.9056456685066223	0.561809778213501	01:26:44
9	0.429235577583313	0.42650479078292847	0.9041541814804077	0.574569582939148	00:29:37
10	0.4423808455467224	0.4270494282245636	0.9030806422233582	0.5719096660614014	00:29:37
11	0.42716923356056213	0.4680996239185333	0.8970706462860107	0.5209901332855225	00:29:35
12	0.41868582367897034	0.4346182346343994	0.8951678276062012	0.5666190385818481	00:29:34
13	0.4456343948841095	0.4336238503456116	0.8965545892715454	0.5586011409759521	00:29:34
14	0.45990267395973206	0.44667744636535645	0.8992006182670593	0.5545905232429504	00:29:37
15	0.4236343204975128	0.4263724088668823	0.9040934443473816	0.5817092061042786	00:29:36

{'accuracy': '9.0415e-01'}

	NoData	1	2
precision	0.954301	0.723499	0.531962
recall	0.943201	0.705301	0.659678
f1	0.948719	0.714284	0.588976

Succeeded at Saturday, December 14, 2024 4:49:32 PM (Elapsed Time: 18 hours 23 minutes 8 seconds)

Training and Validation loss

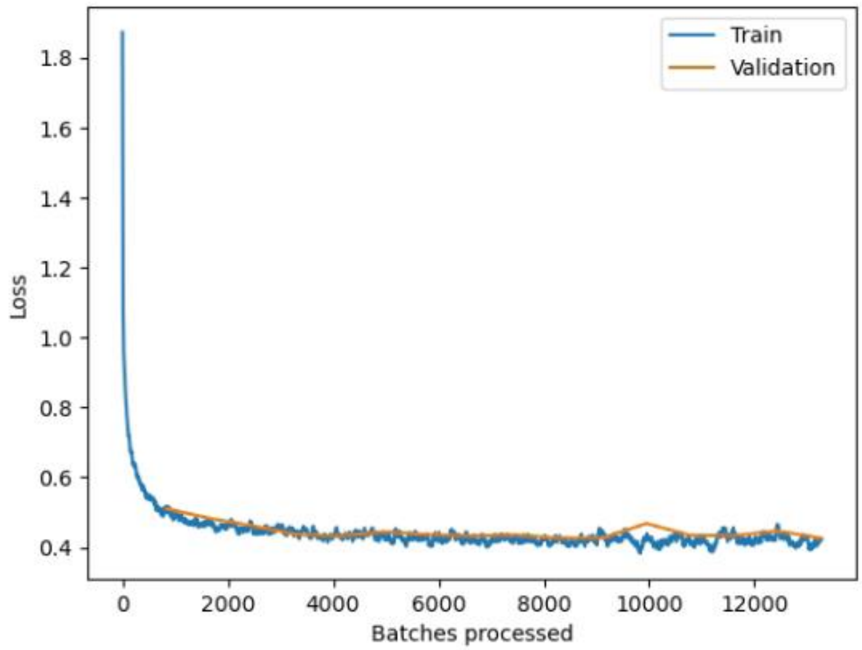

Analysis of the model

Per class metrics:

	NoData	1	2
precision	0.955460	0.720701	0.535171
recall	0.943164	0.714692	0.657753
f1	0.949272	0.717684	0.590164

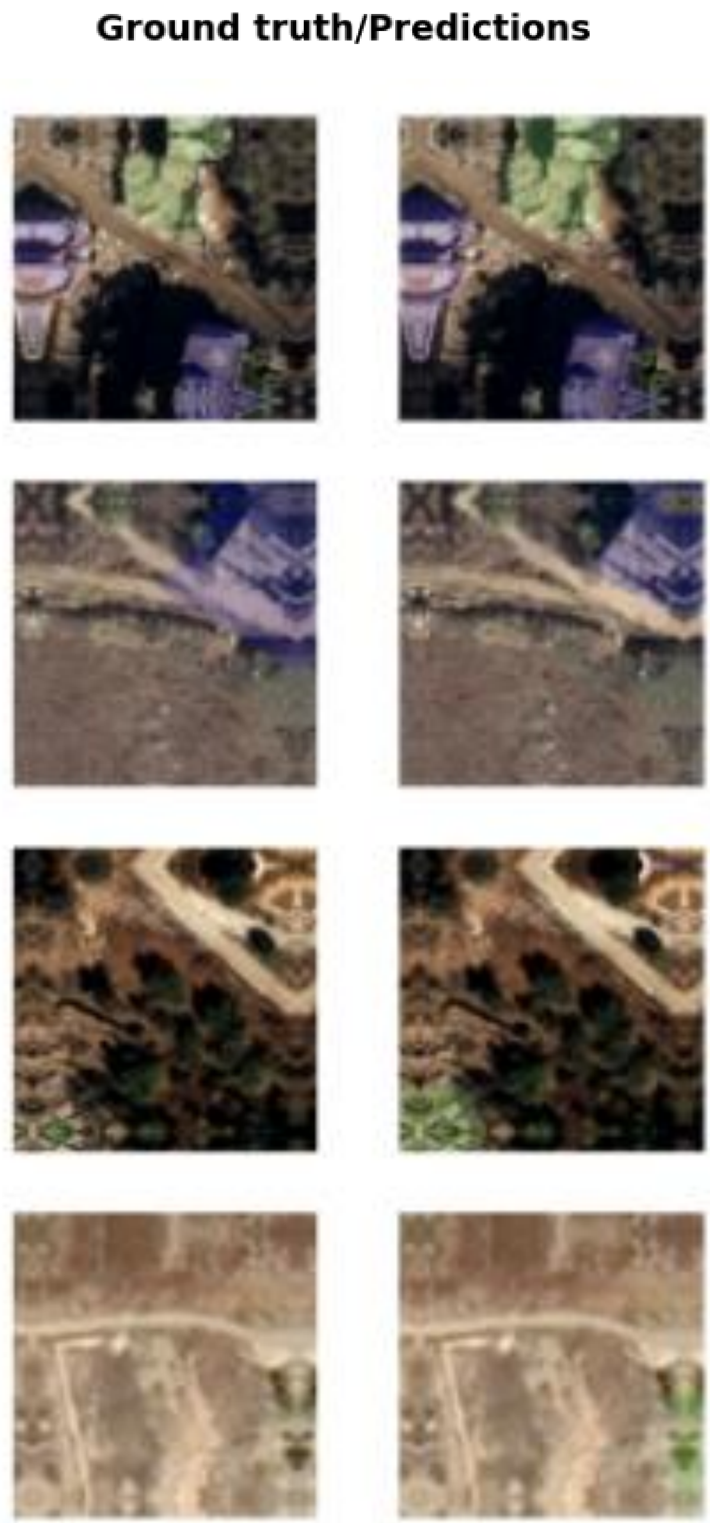
Ground truth/Predictions

Annex 3: Script for Detailed damage detection using Change Detector Architecture for Pixel Classification

```
################Export Training Dataset####################

arcpy.ia.ExportTrainingDataForDeepLearning(
    in_raster=r"Z:\tosamah\mosaic_dataset\HR_Mosaic_03m_R02.tif",
    out_folder=r"E:\Detect_Damage_Samah\Detect_Damage_Pro\Dataset\Dataset_06_128_OR02",
    in_class_data="TOtalDamage1_filtered1",
    image_chip_format="TIFF",
    tile_size_x=128,
    tile_size_y=128,
    stride_x=64,
    stride_y=64,
    output_nofeature_tiles="ONLY_TILES_WITH_FEATURES",
    metadata_format="Classified_Tiles",
    start_index=0,
    class_value_field="class_Nov",
    buffer_radius=0,
    in_mask_polygons=None,
    rotation_angle=0,
    reference_system="MAP_SPACE",
    processing_mode="PROCESS_AS_MOSAICKED_IMAGE",
    blacken_around_feature="NO_BLACKEN",
    crop_mode="FIXED_SIZE",
    in_raster2="Mosaic_Bing_03_R03.tif",
    in_instance_data=None,
    instance_class_value_field=None,
    min_polygon_overlap_ratio=0.2
)

###Final Training model############################

with arcpy.EnvManager(gpuId=1, processorType="GPU"):
with arcpy.EnvManager(gpuId=1, processorType="GPU"):
    arcpy.ia.TrainDeepLearningModel(
        in_folder=r"E:\Detect_Damage_Samah\Detect_Damage_Pro\Dataset\Dataset_06_128_OR02",
        out_folder=r"E:\Detect_Damage_Samah\Detect_Damage_Pro\Model\Model_Res101_DS06_r04",
        max_epochs=100,
        model_type="CHANGEDETECTOR",
        batch_size=8,
        arguments="attention_type PAM;monitor #",
        learning_rate=None,
        backbone_model="RESNET101",
        pretrained_model=None,
        validation_percentage=20,
        stop_training="STOP_TRAINING",
        freeze="UNFREEZE_MODEL",
```

```
    augmentation="DEFAULT",
    augmentation_parameters=None,
    chip_size=128,
    resize_to="",
    weight_init_scheme="",
    monitor="VALID_LOSS"
)
```

Final Model Run:

Train Deep Learning Model
=====================
Tool Path

Input Training Data E:\Detect_Damage_Samah\Detect_Damage_Pro\Dataset\Dataset_06_128_OR02
Output Folder E:\Detect_Damage_Samah\Detect_Damage_Pro\Model\Model_Res101_DS06_r04
Max Epochs 100
Model Type CHANGEDETECTOR
Batch Size 8
Model Arguments attention_type PAM;monitor #
Learning Rate
Backbone Model RESNET101
Pre-trained Model
Validation % 20
Stop when model stops improving STOP_TRAINING
Output Model
E:\Detect_Damage_Samah\Detect_Damage_Pro\Model\Model_Res101_DS06_r04\Model_Res101_DS06_r04.dlpk
Freeze Model UNFREEZE_MODEL
Data Augmentation DEFAULT
Augmentation Parameters
Chip Size 128
Resize To
Weight Initialization Scheme
Monitor Metric VALID_LOSS
=====================
Environments

GPU ID 1
Processor Type GPU
=====================
Messages

Start Time: Monday, December 16, 2024 9:24:28 AM
Learning Rate - slice(2.7542287033381663e-05, 0.0002754228703338166, None)
epoch training loss validation loss precision recall f1_score time
0 1.7945854663848877 481.80633544921875 0.5112951993942261 0.3817768394947052
0.35041505098342896 00:22:24
1 1.3695160150527954 1301.5948486328125 0.6277834177017212 0.37778061628341675
0.3842381536960602 00:20:39
2 1.148319959640503 851.0147094726562 0.6918424963951111 0.36886411905288696
0.41074076294898987 00:20:20
3 1.0463330745697021 270.994873046875 0.7338881492614746 0.3039165735244751
0.363031268119812 00:21:00

4 0.9800031781196594 220.09974670410156 0.7563067674636841 0.24941611289978027
0.3135175406932831 00:21:29
5 0.9353752136230469 160.8945770263672 0.7603453993797302 0.22222620248794556
0.28016477823257446 00:21:46
6 0.8962194919586182 40.31228256225586 0.7673470377922058 0.19101765751838684
0.2537071704864502 00:21:27
7 0.8574151396751404 47.45590591430664 0.76719069480896 0.2209048867225647
0.28626179695129395 00:21:44
8 0.8287486433982849 18.013957977294922 0.7735804319381714 0.252996563911438
0.32466110587120056 00:22:02
9 0.7966465950012207 10.115703582763672 0.7723715305328369 0.3435910940170288
0.4092060625553131 00:21:55
10 0.7779822945594788 2.486483573913574 0.7913402915000916 0.3521668016910553
0.42158353328704834 00:21:49
11 0.7503368258476257 2.0250537395477295 0.7918194532394409 0.4224710166454315
0.4842619001865387 00:21:50
12 0.736775279045105 1.511560082435608 0.7694686651229858 0.33723184466362
0.40197551250457764 00:22:00
13 0.7064321041107178 1.5046559572219849 0.7363307476043701 0.3101016581058502
0.3613913953304291 00:21:45
14 0.7005591988563538 1.4416447877883911 0.7647116184234619 0.34809207916259766
0.41102346777915955 00:21:19
15 0.6973703503608704 1.454820990562439 0.7610014081001282 0.32195550203323364
0.38941437005996704 00:21:28
16 0.6819819211959839 1.457457423210144 0.7586498260498047 0.346473753452301
0.41580745577812195 00:21:30
17 0.6701151728630066 1.396154761314392 0.7409392595291138 0.3822459280490875
0.4412286579608917 00:21:27
18 0.6516273617744446 1.4384392499923706 0.7554007172584534 0.3763667643070221
0.44327980279922485 00:21:22
19 0.6368027925491333 1.2742923498153687 0.7690028548240662 0.5347678661346436
0.5753662586212158 00:21:26
20 0.645839512348175 1.3545546531677246 0.7501475214958191 0.44443294405937195
0.49423569440841675 00:21:24
21 0.623119592666626 1.268798589706421 0.7930842041969299 0.5254139304161072
0.5793293118476868 00:21:27
22 0.6235469579696655 1.3347668647766113 0.786070704460144 0.49309802055358887
0.5534537434577942 00:21:26
23 0.6143074631690979 1.2912254333496094 0.7743745446205139 0.48296058177948
0.5369802713394165 00:21:23
24 0.6001995801925659 1.2074153423309326 0.7642595767974854 0.5600084662437439
0.5936675667762756 00:21:24
25 0.5932406187057495 1.2240374088287354 0.7794204950332642 0.5594837069511414
0.6032918095588684 00:21:31
26 0.5853695869445801 1.1836268901824951 0.787832498550415 0.5870722532272339
0.6232485771179199 00:21:28
27 0.5770547986030579 1.1501941680908203 0.7878942489624023 0.6124416589736938
0.6486144065856934 00:21:27
28 0.5701809525489807 1.169690489768982 0.7963071465492249 0.6119945645332336
0.6523247361183167 00:21:41
29 0.565129816532135 1.059760332107544 0.7747295498847961 0.6882923245429993
0.6917678117752075 00:20:44
30 0.5522595643997192 1.0439109802246094 0.7797606587409973 0.6859106421470642
0.6937831044197083 00:20:30
31 0.5344767570495605 0.9921144247055054 0.7868813872337341 0.7244094610214233
0.7212815284729004 00:20:32

32	0.5295894145965576	0.9963883757591248	0.777101457118988	0.7188956141471863	0.7151180505752563	00:20:24
33	0.530430018901825	0.9625898003578186	0.7827447056770325	0.7384728789329529	0.7335113883018494	00:20:37
34	0.5218715667724609	0.8817358613014221	0.7693506479263306	0.7881144881248474	0.753497302532196	00:20:38
35	0.5125178098678589	0.9784775972366333	0.7913274765014648	0.7343043088912964	0.7350597381591797	00:20:24
36	0.4954493045806885	0.9470604062080383	0.7850302457809448	0.7475892305374146	0.7384707927703857	00:20:33
37	0.48977068066596985	0.903014600276947	0.7702603340148926	0.7719305753707886	0.7445083856582642	00:21:19
38	0.48601529002189636	0.9776532053947449	0.7906134724617004	0.736107587814331	0.7343727946281433	00:21:42
39	0.47370079159736633	0.947394609451294	0.7892990708351135	0.7462137341499329	0.7421233057975769	00:21:39
40	0.4698106348514557	0.9409615397453308	0.7738650441169739	0.7555818557739258	0.7387213706970215	00:21:36

{'precision': 0.7693506479263306, 'recall': 0.7881144881248474, 'f1': 0.753497302532196}
Succeeded at Tuesday, December 17, 2024 12:01:36 AM (Elapsed Time: 14 hours 37 minutes 7 seconds)